Quantitative intra-Golgi transport and organization data suggest the stable compartment nature of the Golgi

Hieng Chiong Tie[1,2,3], Haiyun Wang[1,2], Divyanshu Mahajan[1], Hilbert Yuen In Lam[1], Xiuping Sun[1], Bing Chen[1], Yuguang Mu[1], and Lei Lu[1]

[1]School of Biological Sciences, Nanyang Technological University, Singapore

[2]Equal contribution

[3]Medisix Therapeutics, 11 Biopolis Way, #05-08/09 Helios, Singapore 138667

Keywords

Golgi, membrane trafficking, intra-Golgi transport, cisternal progression model, stable compartment model

*Correspondence should be addressed to:

Lei Lu (PhD)

School of Biological Sciences, Nanyang Technological University, 60 Nanyang Drive, Singapore 637551; Tel: 65-65922591; Fax: 65-67913856; Email: lulei@ntu.edu.sg

Abstract

How the intra-Golgi secretory transport works remains a mystery. The cisternal progression and the stable compartment models have been proposed and are under debate. Classic cisternal progression model posits that both the intra-Golgi transport and Golgi exit of secretory cargos should occur at a constant velocity dictated by the cisternal progression; furthermore, COPI-mediated intra-Golgi retrograde transport is essential for maintaining the Golgi organization. Leveraging our recently developed Golgi imaging tools in nocodazole-induced Golgi ministacks, we found that the intra-Golgi transport velocity of a secretory cargo decreases during their transition from the *cis* to the *trans*-side of the Golgi, and different cargos exhibit distinct velocities even within the same cisternae. We observed a vast variation in the Golgi residence times of different cargos. Remarkably, truncation of the luminal domain causes the Golgi residence time of Tac — a standard transmembrane secretory cargo without intra-Golgi recycling signals — to extend from 16 min to a notable 3.4 h. Additionally, when COPI-mediated intra-Golgi retrograde transport was inhibited by brefeldin A, we found that nocodazole-induced Golgi can remain stacked for over 30 - 60 minutes. Therefore, our findings challenge the classical cisternal progression model and suggest the stable compartment nature of the Golgi.

Introduction

The Golgi complex in mammalian cells plays a crucial role in membrane trafficking and post-translational modification of proteins and lipids (cargos). Centrally positioned around the microtubule organization center(Glick and Luini, 2011; Klumperman, 2011), it comprises laterally connected Golgi stacks, each containing 4 – 7 tightly adjacent membrane sacs known as cisternae. Conventionally, a Golgi stack is recognized to have three regions: the *cis*, medial, and *trans*-Golgi. The *trans*-Golgi network (TGN) assembles outside the *trans*-side of a Golgi stack and is mainly composed of tubular and vesicular membranes(De Matteis and Luini, 2008). In the secretory pathway, newly synthesized cargos exit the ER at the ER exit site (ERES), pass the ER and Golgi intermediate compartment (ERGIC), and reach the Golgi. Cargos subsequently transit from the *cis*-side through the medial and eventually reach the *trans*-side of the Golgi, where they exit the Golgi and target the plasma membrane (Bergmann and Singer, 1983; Castle et al., 1972).

Despite decades of research, the Golgi remains one of the most enigmatic organelles, particularly regarding the mechanism of intra-Golgi transport of secretory cargos(Emr et al., 2009; Glick and Luini, 2011). Two primary intra-Golgi transport models have been proposed and are currently the subject of debate. In the classic cisternal progression or maturation model, secretory cargos passively reside within Golgi cisternae, which progress or mature from the *cis* to the *trans*-Golgi cisternae to facilitate the forward or anterograde transport of cargos. Simultaneously, post-translational modification enzymes such as glycosyltransferases move in reverse or retrograde transport, altering cisternal properties to become the next cisternae of the Golgi stack. Under this perspective, the Golgi functions at a dynamic equilibrium of anterograde and retrograde intra-Golgi transport. The model predicts that all secretory cargos should have the same and constant intra-Golgi transport and Golgi exit velocity. It can provide a plausible explanation for the intra-Golgi transition of oversized secretory cargos, such as procollagen I (Bonfanti et al., 1998; Mironov et al., 2001). Moreover, direct observations of cisternal maturation have been made in budding yeast *Saccharomyces*

cerevisiae(Kurokawa et al., 2019; Losev et al., 2006; Matsuura-Tokita et al., 2006), although similar observation has not been reported in mammalian cells. However, the budding yeast Golgi differs significantly from the mammalian one in the cisternal organization – it scatters throughout the cytoplasm as unstacked compartments. This substantial difference casts doubt on the general applicability of the budding yeast Golgi observation to higher eukaryotes.

In contrast, the stable compartment model posits that Golgi cisternae are stable entities. During intra-Golgi transport, carriers actively move secretory cargos from one cisterna or compartment to the next, from the *cis* to the *trans*-side, while post-translational modification enzymes remain stationary. At the *trans*-side of the Golgi, cargos are sorted into carriers bound for the plasma membrane. As a result, different cargos can exhibit distinct intra-Golgi transport and Golgi exit velocities under this model. To account for the intra-Golgi transport of oversized secretory cargos, such as procollagen I, a modified version of the stable compartment model, the rim progression model, has been proposed (Lavieu et al., 2013; Pfeffer, 2010; Volchuk et al., 2000). In this model, each Golgi cisterna seems to have a stable interior domain and a dynamic rim domain; the rim domain of Golgi cisternae undergoes constant en bloc fission and fusion, carrying small or large cargos to the next cisternae for intra-Golgi cargo transport. The rim partitioning of large secretory cargos is supported with previous EM studies of procollagen I(Bonfanti et al., 1998), FM4 aggregates(Lavieu et al., 2013), and algal protein aggregates(Engel et al., 2015). Furthermore, we have recently demonstrated in fluorescence microscopy that during their intra-Golgi transition, small cargos, such as CD59, E-cadherin, and VSVG, localize to the cisternal interior, coinciding with Golgi glycosyltransferases, while large cargos, such as FM4 aggregates and collagenX, position themselves at the cisternal rim, where trafficking machinery components localize(Tie et al., 2018).

Once secretory cargos transit the Golgi stack, they reach the *trans*-side of the Golgi and are packed into carriers destined for the plasma membrane. The classic cisternal progression model posits that secretory cargos linearly depart the *trans*-Golgi. Contrary to this, cargo exit

kinetics have been shown to adhere to a first-order exponential relationship rather than a linear one(Hirschberg et al., 1998; Patterson et al., 2008; Sun et al., 2020). In an attempt to reconcile these observations, Patterson *et al*. introduced the rapid partitioning model, which stands distinct from the classic cisternal progression and stable compartment models(Patterson et al., 2008). This model suggests that cargos rapidly diffuse throughout the Golgi stack, segregating into multiple post-translational processing and export domains, where cargos are packed into carriers bound for the plasma membrane. Nonetheless, synchronized traffic waves have been observed through various techniques, including electron microscopy (EM)(Trucco et al., 2004) and advanced light microscopy methods we developed, such as GLIM and side-averaging(Tie et al., 2016; Tie et al., 2022). These findings suggest that the rapid partitioning model might not accurately represent the true nature of the intra-Golgi transport.

The ongoing debate among these models underscores the complexity of the Golgi and reflects the insufficiency of the existing experimental data, especially the intra-Golgi transport kinetics data. Two semi-quantitative approaches exist for studying the intra-Golgi transport kinetics of ER-synchronized secretory cargos. The first is the biochemical approach, where intra-Golgi transport kinetics can be indirectly deduced by subtracting ER-to-Golgi and Golgi-to-plasma membrane transport from the overall secretion (ER-to-plasma membrane transport) during the chase(Ernst et al., 2018). However, this indirect approach provides only an averaged intra-Golgi transport kinetics, making it incapable of measuring the instantaneous intra-Golgi transport velocity at a sub-Golgi region. The second approach involves EM imaging of immuno-gold labeled secretory cargos at Golgi cisternae(Beznoussenko et al., 2014; Trucco et al., 2004). The distribution of gold particles among individual Golgi cisternae during the chase directly indicates intra-Golgi transport kinetics. Nevertheless, this approach demands specialized techniques and equipment and considerable manual work in EM imaging and subsequent image examination, limiting its widespread use in other labs.

The limitations in current approaches call for novel methods, especially ones based on fluorescence microscopy, to resolve the intra-Golgi transport spatially and kinetically. However,

optically resolving the intra-Golgi secretory transport in mammalian cells is challenging due to the thinness (200 – 400 nm) and random orientation of Golgi stacks. To overcome this, we leverage the uniform and rotationally symmetrical arrangement of nocodazole-induced Golgi ministacks (hereafter referred to as Golgi ministacks). Extensive studies have provided strong evidence that ministacks obtained under prolonged nocodazole treatment ($\geq$ 3 h), the condition employed in our studies, largely represent the native Golgi stack(Cole et al., 1996; Fourriere et al., 2016; Rogalski et al., 1984; Schueder et al., 2024; Tie et al., 2018; Trucco et al., 2004; Van De Moortele et al., 1993). We developed a numerical Golgi localization tool called Golgi localization by imaging centers of mass (GLIM) that can precisely pinpoint a Golgi protein's cisternal localization with nanometer accuracy in Golgi ministacks(Tie et al., 2017; Tie et al., 2016). Alongside this, we propose using the metric of Golgi residence time to quantify a Golgi protein's retention in the Golgi(Sun et al., 2021; Sun et al., 2020).

Here, we utilized past and newly acquired GLIM and Golgi residence time data to quantitatively analyze intra-Golgi transport and Golgi exit kinetics. Our data revealed that neither intra-Golgi transport nor Golgi exit exhibits a constant velocity. We discovered that when the luminal domain of Tac — a conventional transmembrane secretory cargo lacking intra-Golgi recycling signals — is truncated, its Golgi residence time increases from 16 min to a substantial 3.4 h. Through GLIM, we examined the cisternal organization of Golgi ministacks under brefeldin A (BFA) treatment, which halts retrograde intra-Golgi transport. Remarkably, under this condition, we found that nocodazole-induced Golgi ministacks can remain stacked for 30 - 60 min. Therefore, our findings underscore the stable compartment nature of Golgi cisternae. They challenge the classical cisternal progression model and favor the stable compartment model.

Results and discussion

The intra-Golgi transport is not a motion with constant velocity

The classic cisternal progression model postulates that the intra-Golgi transport velocity of a secretory cargo should remain constant. However, this prediction has not been directly tested due to the inherent challenge of measuring the intra-Golgi transport velocity. The advent of GLIM has allowed us to address this issue. In GLIM, briefly, HeLa cells expressing the RUSH secretory cargo (RUSH reporter)(Boncompain et al., 2012) and GalT-mCherry, a *trans*-Golgi marker containing amino acids 1-81 of B4GALT1, were initially treated with nocodazole. Subsequently, cells were chased in biotin with nocodazole and cycloheximide (a protein synthesis inhibitor) for various lengths of time (*t*) before immunofluorescence labeling for endogenous GM130, a *cis*-Golgi marker. Additionally, apart from SBP-GFP, a soluble secretory protein, and SBP-GFP-CD59(Tie et al., 2016), a glycosylphosphatidylinositol-anchored protein, all RUSH reporters in this study are transmembrane proteins, including TNFα-SBP-GFP, TfR-SBP-GFP(Chen et al., 2017), SBP-GFP-CD8a-furin-WT(Tie et al., 2016), SBP-GFP-CD8a-furin-YA, SBP-GFP-CD8a-furin-AC(Tie et al., 2016), SBP-GFP-CD8a-furin-Y+AC(Tie et al., 2016), SBP-GFP-Tac(Sun et al., 2020), SBP-GFP-Tac-TC(Sun et al., 2020), and SBP-GFP-E-cadherin(Boncompain et al., 2012). Except for TNFα-SBP-GFP, which uses Ii-streptavidin as the ER hook, all RUSH reporters employ signal sequence fused streptavidin-KDEL as their ER hook (Fig. 1).

We calculated centers of mass as the positions of GM130, RUSH reporter, and GalT-mCherry within each analyzable Golgi ministack. The RUSH reporter's Golgi localization quotient, or *LQ*, is calculated by dividing its distance from GM130 by GalT-mCherry's distance from GM130 (Supplementary Fig. 1 A-G). The *LQ* is a linear numerical metric to indicate a cargo's axial localization within the Golgi, with a nanometer range of precision(Tie et al., 2017; Tie et al., 2016). We previously linearly defined regions of Golgi: ERES/ERGIC ($LQ < -0.25$), *cis* ($-0.25 \leq LQ < 0.25$), medial ($0.25 \leq LQ < 0.75$), *trans*-Golgi ($0.75 \leq LQ < 1.25$), and TGN ($LQ \geq 1.25$).

To analyze the intra-Golgi transport kinetics of secretory cargos, we measured the *LQ*s of RUSH reporters after various durations of biotin administration (chase). Most kinetic data was previously reported in HeLa cells (Tie et al., 2017; Tie et al., 2016) and re-analyzed here. Additionally, we generated new data and replicated specific measurements. GLIM involves laborious manual image analysis. To increase image analysis efficiency, we developed a software tool, Auto-GLIM, to automatically analyze ministack images and calculate *LQ*s by using a deep learning algorithm (the manuscript will be published elsewhere). We found that Auto-GLIM can produce *LQ*s similar to the conventional manual analysis method (Supplementary Fig. 1 H-M) but requires much less user interaction, therefore increasing our image analysis efficiency. We employed the Auto-GLIM tool to analyze the intra-Golgi transport of RUSH reporters, SBP-GFP-CD59 and SBP-GFP-Tac-TC, in HEK293T cells.

Figure 2, Supplementary Figure 2, and Supplementary File 1 illustrate that our *LQ* vs. *t* plots are highly reproducible. As previously reported, all *LQ* vs. *t* plots fit the following first-order exponential function (Equation 1) well with an adjusted R^2 (adj. R^2) ≥ 0.85 (Fig. 2A-J and Supplementary Fig. 2A-T, left panels).

$$LQ = y_0 - Ae^{\left(-\frac{ln2}{t_{intra}}t\right)} \qquad \text{(Equation 1)}$$

In Equation 1, *t* represents chase time in minutes (biotin treatment starts at *t* = 0); *ln*2 is the natural logarithm of 2; *A* is a constant; y_0 represents the *LQ* of the Golgi exit site; t_{intra} is the time that the cargo reaches half of the transport range and is hereafter referred to as the intra-Golgi transport time. Table 1 lists t_{intra}, y_0, and adj. R^2 of each data set. We define the instantaneous intra-Golgi transport velocity as the derivative of *LQ* with respect to time, *dLQ/dt*, which measures the axial transport velocity of the center of mass of the synchronized cargo wave. It should also follow the first-order exponential function (Equation 2).

$$\frac{dLQ}{dt} = \frac{Aln2}{t_{intra}} e^{\left(-\frac{ln2}{t_{intra}}t\right)} \qquad \text{(Equation 2)}$$

In this context, the intra-Golgi transport velocity is the highest when the cargo enters the secretory pathway ($t = 0$). However, it is crucial to approach this extrapolation cautiously due to the lack of experimental data at $t \leq 5$ min, when a RUSH reporter's high ER background and low Golgi signal make it challenging to select analyzable Golgi ministacks. It is evident that the *dLQ/dt* of all our RUSH reporters slows to zero as they transit across the Golgi stack to reach $LQ = y_0$ at the *trans*-Golgi or TGN (Fig. 2A-J and Supplementary Fig. 2A-T, right panels). At the *trans*-Golgi, we propose that RUSH reporters that do not target the TGN exit Golgi ministacks in carriers en route to the plasma membrane(Tie et al., 2018; Tie et al., 2016; Tie et al., 2022). Hence, the intra-Golgi transport velocity of a secretory cargo does not remain constant, contradicting the prediction of the classic cisternal progression model.

The intra-Golgi transport kinetics of collagenX, a cisternal rim partitioned secretory cargo, resemble those of conventional cargos

CollagenX has been known to assemble into oligomers(Kwan et al., 1991). We previously reported that the collagenX RUSH reporter, SBP-GFP-collagenX, forms large aggregates containing ~ 190 copies(Tie et al., 2018). With an estimated mean size of ~ 40 nm, these aggregates are much smaller than FM4 aggregates and procollagen I (> 300 nm)(Bonfanti et al., 1998; Volchuk et al., 2000) and, therefore, are not excluded from conventional transport vesicles, which typically have a size of 50 – 100 nm. However, our previous findings showed that while conventional secretory cargos partition to the cisternal interior during intra-Golgi transport, large cargos such as FM4 aggregates and collagenX preferentially localize to the cisternal rim(Tie et al., 2018), highlighting distinct intra-Golgi transport behavior for different cargo sizes. Hence, we asked if collagenX follows the same intra-Golgi transport kinetics as conventional secretory cargos.

Using the RUSH assay, our *LQ* vs. *t* data demonstrated that the intra-Golgi transport of SBP-GFP-collagenX followed a first-order exponential function, with a t_{intra} of 8 ± 1 (mean ± *SD*, $n = 3$) (Fig. 3 A-C; Table 1). SBP-GFP-collagenX exited at the *trans*-Golgi, with a y_0 of 0.92 ± 0.08 (mean ± *SD*, $n = 3$). Additionally, the instantaneous intra-Golgi transport velocity (*dLQ/dt*)

of SBP-GFP-collagenX also decreases in accordance with a first-order exponential function (Fig. 3 A-C; Table 1).

Using side averaging, we visualized the synchronized traffic wave of SBP-GFP-collagenX as it transitioned across the ministack (Fig. 3 D and E; Supplementary Fig. 3). When passing through the medial and *trans*-Golgi regions at *t* = 10 and 20 min after biotin chase, SBP-GFP-collagenX appeared as double puncta, supporting its cisternal rim localization (Fig. 3 D). 40 min after biotin chase, numerous SBP-GFP-collagenX-positive carriers were observed surrounding the *trans*-Golgi, indicating a process of Golgi exiting (Fig. 3 D). In summary, our findings demonstrated that cisternal rim partitioned large size secretory cargos might follow intra-Golgi transport kinetics similar to those of cisternal interior partitioned conventional secretory cargos.

Distinct intra-Golgi transport velocities for different cargos at the same cisternae

From Equations 1 and 2, we derive the following relationship (Equation 3):

$$\frac{dLQ}{dt} = \frac{ln2}{t_{intra}}(y_0 - LQ) \qquad \text{(Equation 3)}$$

In our previous work, through side-averaging, we determined that one *LQ* unit corresponds to 274 nm (Tie et al., 2022). Hence, we scaled Equation 3 by 274 nm to derive the instantaneous intra-Golgi transport velocity in nm/min. When plotting the instantaneous intra-Golgi transport velocity (nm/min) against the *LQ* for selected RUSH reporters, as seen in Figure 4A, we observed that different secretory cargos exhibit varied transport velocities even within the same cisternae or at the same *LQ* values. At *LQ* = 0.40, corresponding to the medial-Golgi region, our RUSH reporters' instantaneous intra-Golgi transport velocities are calculated in Table 1 according to Equation 3. For instance, instantaneous intra-Golgi transport velocities of SBP-GFP, SBP-GFP-Tac-TC, SBP-GFP-CD59, SBP-GFP-Tac, and TNFα-SBP-GFP are 6.1, 8.0, 9.2, 14.6, and 20.5 nm/min, respectively (Table 1). These findings highlighted that different secretory cargos possess distinct intra-Golgi transport velocities within the same Golgi cisternae, challenging the prediction made by the classic cisternal progression model.

Golgi residence times vary significantly among different secretory cargos

Once cargos transit through the Golgi stack, the classic cisternal progression model predicts that cargos depart the Golgi in a linear kinetics. However, studies have demonstrated that cargos exit the Golgi by following the first-order exponential kinetics(Hirschberg et al., 1998; Patterson et al., 2008; Sun et al., 2020). While we could apply a hypothetical rate-limiting step to the classic cisternal progression and stable compartment models to rationalize the exponential kinetics of cargo exit(Luini, 2011), the classic cisternal progression model encounters more significant challenges. Firstly, the first-order exponential Golgi exit implies that clearing a synchronized wave of secretory cargo from the *trans*-cisternae would take an indefinite time, which is inconsistent with the transient nature of the *trans*-cisternae as described by the classic cisternal progression model. Secondly, since cargos are considered passive in the classic cisternal progression model, the exit kinetics, as measured by the Golgi residence times, should be the same across all secretory cargos.

The Golgi residence time is a cargo's duration at the *trans*-Golgi cisternae before exit and is a metric for Golgi retention(Sun et al., 2021; Sun et al., 2020). The first step to determine this metric involves synchronizing a transmembrane protein at the Golgi. For Golgi transmembrane resident proteins like glycosyltransferases and secretory transmembrane proteins with a substantial Golgi localization at the steady state, such as GFP-Tac-TC, synchronization is not required. However, for secretory transmembrane cargos lacking a significant Golgi pool at the steady state, such as TfR-GFP, GFP-Tac, and RUSH reporters like TNFα-SBP-GFP, synchronization is achieved through a 20°C temperature block. Subsequently, live imaging at 37 °C is performed to capture the Golgi fluorescence intensity decay of the protein in the presence of cycloheximide. The Golgi residence time is calculated as the half-time ($t_{1/2}$) by fitting the intensity decay to a first-order exponential function.

Our extensive measurement demonstrated that Golgi residence times of secretory cargos display a wide range of values (Table 2). For example, TNFα-SBP-GFP has a Golgi residence time of 6.0 ± 0.4 min (mean ± SEM, n = 73), one of the shortest, while SBP-GFP-CD59 has a

Golgi residence time of 16 ± 2 min (mean ± SEM, *n* = 29) (Supplementary Fig. 4A). Hence, our data suggest that different secretory cargos reside at the *trans*-Golgi cisternae for varying durations, contradicting predictions from the classic cisternal progression model.

Cargos exhibiting prolonged Golgi residence times suggest the *trans*-Golgi interior might be a stable domain

The classic cisternal progression model could be modified to explain the diverse intra-Golgi transport kinetics. For example, accelerated anterograde or retrograde transport might be introduced on top of the basal cisternal progression to account for the wide range of intra-Golgi transport velocities and Golgi residence times we observed (Fig. 4B). Accelerated anterograde transport mechanisms might include continuity-based direct diffusion across cisternae via heterologous cisternal connections(Beznoussenko et al., 2014; Marsh et al., 2004; Trucco et al., 2004). Hence, secretory cargo with such a mechanism would have a faster intra-Golgi transport velocity. This mechanism might explain the rapid and diverse intra-Golgi transport velocity of secretory cargos such as VSVG, insulin, albumin, and alpha1-antitrypsin(Beznoussenko et al., 2014; Marsh et al., 2004; Trucco et al., 2004). Similarly, active recruitment to exocytic carriers budding at the *trans*-Golgi possibly might shorten the Golgi residence time. On the other hand, COPI-coated carriers might facilitate retrograde intra-Golgi transport to counter the cisternal progression, accounting for the slow intra-Golgi transport velocity and prolonged Golgi residence time of cargos. Indeed, COPI has been known to maintain certain glycosyltransferases' Golgi retention by direct or indirect interactions (Ali et al., 2012; Eckert et al., 2014; Liu et al., 2018; Pereira et al., 2014; Rizzo et al., 2021; Schmitz et al., 2008; Tu et al., 2008). However, such a retrograde mechanism requires the interaction between secretory cargo and the COPI coat.

Earlier, we identified truncation mutants of two typical secretory cargos, GFP-Tac(Sun et al., 2020) and GFP-CD8a, which reside in the Golgi nearly as stably as Golgi glycosyltransferases. GFP-Tac and GFP-CD8a are type I transmembrane proteins comprising from their N- to C-termini a signal sequence, GFP, luminal domain, transmembrane domain (TMD), and

cytosolic tail (Fig. 5A). Previously, we and others demonstrated that fully glycosylated luminal domain can function as a Golgi exit signal (Gut et al., 1998; Sun et al., 2020). Their Golgi residence time was documented at 16 ± 2 min (mean ± SEM, *n* = 45) and 7.8 ± 0.7 min (mean ± SEM, *n* = 26), respectively (Table 2). However, after truncating the luminal domain, the Golgi residence time for the resultant chimeras, GFP-Tac-TC and GFP-CD8a-TC, extended significantly to 3.4 ± 0.3 h (mean ± SEM, *n* = 22) and 66 ± 7 min (mean ± SEM, *n* = 19) (Table 2)(Supplementary Fig. 4B), respectively. Consequentially, their long Golgi residence times ensure a significant steady-state Golgi pool.

The following evidence suggests that GFP-Tac-TC and GFP-CD8a-TC behave like bona fide Golgi resident transmembrane proteins. Firstly, their Golgi residence times, 3.4 h and 66 min, are comparable to that of a typical Golgi glycosyltransferase, such as ST6GAL1 (5.3 ± 0.6 h, mean ± SEM, *n* = 21)(Sun et al., 2021). Second, their *LQ*s, 0.94 ± 0.02 (mean ± SEM, *n* = 118) and 0.86 ± 0.05 (mean ± SEM, *n* = 76), combined with their cisternal interior localization (Fig. 5B)(Sun et al., 2020), indicate that they primarily reside within the interior of the *trans*-cisternae, similar to many Golgi glycosyltransferases(Tie et al., 2018). Additionally, GFP-Tac-TC follows GalT-mCherry to localize to the ER under the BFA treatment reversibly (Sun et al., 2020).

According to the modified cisternal progression model above, GFP-Tac-Tc could have an active retrieval mechanism mediated by an unidentified signal in its cytosolic tail or TMD to counter the cisternal progression. Considering that GFP-Tac-TC's *LQ* (0.94) is close to its Golgi exit site, y_0 (0.95 – 1.16) (Table 1; Fig. 2G,H and Supplementary Fig. 2M-O), measured by its RUSH version, there are two possible retrieval pathways, acting at either post-Golgi or intra-Golgi stages. To test if GFP-Tac-Tc possesses a Golgi retrieval pathway after its Golgi exit, we incubated HeLa cells transiently expressing MGAT1-GFP (negative control)(Sun et al., 2021), MGAT2-GFP (positive control)(Sun et al., 2021), GFP-Tac, or GFP-Tac-TC with a recombinant mCherry-fused anti-GFP nanobody (VHH-anti-GFP-mCherry) continuously for 8 h (Fig. 5C). By binding to the cell surface-exposed GFP, VHH-anti-GFP-mCherry serves as a

sensitive probe to track the endocytic trafficking itinerary of the above GFP-fused transmembrane proteins.

We found that VHH-anti-GFP-mCherry localized to the Golgi in a significant fraction of MAGT2-GFP-expressing cells (32%, *n* = 266) but not in MGAT1-GFP cells (0%, *n* = 102) after 8 h continuous internalization (Fig. 5C). This result is consistent with our previous report that MGAT2, but not MAGT1, has a Golgi retrieval mechanism(Sun et al., 2021), although its molecular mechanism is still unknown. In contrast, VHH-anti-GFP-mCherry did not localize to the Golgi in cells expressing other constructs, including GFP-Tac-TC, suggesting that GFP-Tac-TC might not possess a post-Golgi retrieval mechanism targeting the Golgi (Fig. 5C). Next, we reason that given GFP-Tac's short Golgi residence time (16 min), its cytosolic tail and TMD might not facilitate any active intra-Golgi retrograde transport mechanism, such as COPI coat binding, to recycle GFP-Tac-TC from Golgi exiting. Since GFP-Tac and GFP-Tac-TC share identical TMD and cytosolic tail sequences, if such a retrograde mechanism existed, GFP-Tac would have a similar Golgi residence time to GFP-Tac-TC. The same observation and reasoning also apply to GFP-CD8a-TC (Fig. 5C).

Therefore, we argue that GFP-Tac-TC and GFP-CD8a-TC might not have retrieval signals to facilitate their Golgi residence, although proving a protein does not possess a transport signal is challenging. Since the cisternal interior is continuous with the cisternal rim both in membrane and lumen, our findings suggest that the cisternal interior at the *trans*-Golgi might be a stable domain. In summary, our data implies that retention within the *trans*-side stable domain, rather than continuous retrieval to counter the cisternal progression (treadmilling), could be the primary mechanism for the long Golgi residence times of GFP-Tac-TC and GFP-CD8a-TC.

The Golgi maintains its stacked organization after 30 min BFA treatment

COPI functions in the retrograde direction at the ER-Golgi interface and within the Golgi (Glick and Luini, 2011; Popoff et al., 2011; Rabouille and Klumperman, 2005). According to the classic cisternal progression model, COPI-mediated retrograde intra-Golgi transport recycles

resident transmembrane proteins, such as glycosyltransferases and transport machinery components. This model predicts that upon the compromise of COPI, intra-Golgi recycling would stop, and the Golgi stack would continuously lose its materials and eventually disappear, depending on the cisternal progression rate. In addition to its retrograde role, COPI has also been documented to function in the anterograde ER-to-Golgi transport(Monetta et al., 2007; Weigel et al., 2021).

To test the role of COPI in the Golgi organization, we employed BFA, a small molecule fungal metabolite that rapidly dissociates COPI and clathrin from the Golgi, inhibits the ER-to-Golgi trafficking, and causes the fusion of the Golgi with the ER in 10 - 20 min(Klausner et al., 1992). It does so by rapidly inactivating class I ARFs, which recruit COPI and clathrin coats to the Golgi membrane(Donaldson et al., 1992; Helms and Rothman, 1992). In contrast to the native Golgi, nocodazole-induced Golgi ministacks have been documented to be more resistant to BFA, and, hence, the disappearance of Golgi occurs at a much later time (> 30 min)(Lippincott-Schwartz et al., 1990). However, it is unclear if the nocodazole-induced Golgi maintains a similar stacked organization under the BFA treatment.

To address this, we studied the *LQ*s of several Golgi markers following 30 – 60 min of BFA treatment (Fig. 6A-E and Supplementary Fig. 5A,B). The fast dissociation of Arf1-GFP from Golgi ministacks confirmed the effectiveness of BFA (Supplementary Fig. 5A). We also observed that extended BFA treatment considerably reduced the number of intact Golgi ministacks. We measured the *LQ*s of six transmembrane Golgi markers, GFP-golgin-84, GS15, ST6GAL1-GFP, TGN46, CD8a-furin, and CD8a-CI-M6PR (Fig. 6A-F and Supplementary Fig. 5B). GS15's *LQ* was monitored for 60 min, with the rest for 30 min. Strikingly, we observed that Golgi puncta are still stacked as all measured *LQ*s exhibited a relative arrangement similar to those of the pre-BFA treatment (t = 0 min) (Fig. 6F). For example, *LQ*s of ST6GAL1 and GS15 remained largely unchanged after 30 min BFA treatment. Although the *LQ* of golgin-84 increased from 0.2 to 0.4, it still remained between the *LQ*s of

GM130 and GS15. The stacked organization of BFA-treated ministacks was further confirmed by the side-averaging images of GM130, Giantin, GalT-mCherry, and CD8a-furin (Fig. 6G,H).

However, BFA treatment altered the physical dimensions of ministacks. We defined the distance between two Golgi markers as the distance between their Gaussian peak centers in the axial line intensity profile (see the Materials and Methods). We observed the distance from GM130 to GalT-mCherry, $d_{(\text{GM130-GalT-mCherry})}$, decreased from 300 ± 10 nm (mean ± SEM, n = 34) to 190 ± 30 (mean ± SEM, n = 13) after 30 min of BFA treatment, indicating axial shrinkage of ministacks (Fig. 6G). Furthermore, *LQ*s of all three TGN markers, TGN46, CD8a-furin, and CD8a-CI-M6PR, decreased and approached that of the *trans*-Golgi, suggesting a collapse of the TGN (Fig. 6F), possibly due to the dissociation of clathrin and its adaptor proteins. This collapse of the TGN was further supported by the side-averaging images, in which CD8a-furin gradually approached the *trans*-Golgi labeled by GalT-mCherry over time (Fig. 6H). We found the distance from GalT-mCherry to CD8a-furin, $d_{(\text{GalT-mCherry-CD8a-furin})}$, decreased from 200 ± 20 nm (mean ± SEM, n = 30) to 100 ± 30 nm (mean ± SEM, n = 20) after 30 min of BFA treatment.

Despite dramatic changes in the TGN and shrinkage of the axial length of the Golgi minitack, our data demonstrate that the Golgi maintains its stacked organization for at least 30 – 60 min, even in the absence of COPI-mediated intra-Golgi retrograde transport. Our findings suggest that the Golgi might not be a dynamic equilibrium between the cisternal progression and retrograde trafficking and argue for a by-default stable nature of the Golgi stack. It is worth noting that the cellular effect of BFA is complex and pleiotropic. For example, in addition to Arfs, it can inhibit lipid metabolic enzymes(De Matteis et al., 1994). So, the disassociation of COPI might not be the sole factor responsible for our observations.

Our data supports the rim progression model, a modified version of the stable compartment model

Previously, we discovered that Golgi glycosyltransferases tend to localize to the cisternal interior, while trafficking machinery components localize primarily to the cisternal rim(Tie et al.,

2018). Combined with our current observations of differential intra-Golgi transport velocities among distinct secretory cargos (Fig. 2-4 and Supplementary Fig. 2) and the stable *trans*-Golgi interior localization of GFP-Tac-TC(Sun et al., 2020) and GFP-CD8a-TC (Fig. 5B and Table 2), these findings support the modified version of the stable compartment model – the rim progression model. This model explains the retention of Golgi glycosyltransferases in the cisternal interior, given that many do not recycle via COPI-coated vesicles(Liu et al., 2018) or possess a post-Golgi retrieval pathway(Sun et al., 2021). It also readily accounts for the diverse intra-Golgi transport velocities of secretory cargos by suggesting that each cargo type may have a different retention time within the stable cisternal interior domain.

The Golgi glycosyltransferases at the cisternal interior might assemble a dense protein matrix based on fluorescence microscopy(Tie et al., 2018) and EM data(Engel et al., 2015). It is tempting to speculate that the enzyme matrix could provide the molecular basis for the stable cisternal interior domain and functionally mirror a gel-filtration chromatography matrix with a defined porosity. Hence, large secretory cargos, such as FM4 aggregates and collagenX, are excluded from the interior, where the enzyme matrix localizes, while small secretory cargos can enter and become kinetically trapped there. The progressive reduction in intra-Golgi transport of secretory cargo might result from the enzyme matrix's retention at the *trans*-Golgi. As the secretory cargos progress along the Golgi stack from the *cis* to the *trans*-side, more and more cargos become temporarily retained in the *trans*-Golgi region, gradually reducing their overall intra-Golgi transport velocity. If the release or Golgi exit of these cargos from the enzyme matrix follows a constant probability per unit time, i.e., a first-order kinetics process, the rate of cargo exiting from the Golgi should follow the first-order exponential function. Since the mechanism underlying intra-Golgi transport kinetics reflects fundamental molecular and cellular processes of the Golgi, further experimental data are essential to rigorously test this hypothesis.

Limitations of the study

We introduced new quantitative data on the intra-Golgi transport dynamics. However, our study has limitations. First, our approach relied on the overexpression of fluorescence protein-tagged cargos. The synchronized release of a large amount of cargo could significantly saturate and skew the intra-Golgi transport. Second, we utilized nocodazole-induced ministacks instead of the native Golgi to analyze the intra-Golgi transport, which could raise concerns about the impact of depolymerizing microtubules on the intra-Golgi transport and Golgi organization. Third, with the exception of furin and its mutants, all RUSH reporters used in this study are constitutive secretory cargos. As a result, the intra-Golgi transport dynamics observed here might not reflect those of regulated secretion, which involves the synchronized release of a large quantity of cargo in response to a specific signal.

Our findings suggest that the Golgi cisternal interior might be a stable domain, therefore supporting a modified version of the stable compartment model, the rim progression model. However, we do not think our data alone can resolve the two models, which have been the subject of debate for several decades. Further refinement of the classic cisternal progression model might also account for our data. We anticipate further development using our approach will provide more systematic data to test and refine future intra-Golgi transport models. Moreover, we hope that our study will stimulate further research into this longstanding and intriguing question.

Materials and methods

DNA plasmids, antibodies, and small molecules

To clone RUSH reporter, SBP-GFP, two PCRs were performed using li-Strep_ss-SBP-EGFP-Ecadherin (a gift plasmid from F. Perez) (Boncompain et al., 2012) and pEGFP-C1 (Clontech) as templates and the following primer pairs (GAT GCA CCC GGG AGG CGC GCC ATG and CTC CTC GCC CTT GCT CAC ACC TGC AGG TGG TTC ACG) and (CGT GAA CCA CCT GCA GGT GTG AGC AAG GGC GAG GAG and GAT GCA TCT AGA TTA CTT GTA CAG CTC GTC CAT), respectively. The mixture of the two purified PCR fragments was used as the template for the third round of PCR amplification using the first and the fourth primer listed above. The resulting PCR fragment was digested by XmaI and XbaI and ligated to XmaI and XbaI digested li-Strep_ss-SBP-EGFP-Ecadherin DNA plasmid. To clone GFP-CD8a-TC, the coding sequence of the TMD and cytosolic tail of CD8a was amplified by PCR using GFP-CD8a(Sun et al., 2020) as a template and the following primers, CAG TGC CTC GAG GAC TTC GCC TGT GAT ATC TA and GAC CGT GAA TTC TTA GAC GTA TCT CGC CGA AAG GCT G. The resulting PCR fragment was digested by EcoRI and XhoI and ligated to EcoRI and XhoI digested GFP-CD8a DNA plasmid.

ST6GAL1-GFP (ST-GFP) (Sun et al., 2020), CD8a-furin(Mahajan et al., 2013), CD8a-CI-M6PR(Mahajan et al., 2013) were previously described. RUSH TfR-SBP-GFP was a gift plasmid from J. Bonifacino (Chen et al., 2017). GFP-golgin-84 (Diao et al., 2003) was a gift plasmid from M. Lowe. Arf1-GFP(Wessels et al., 2006) was a gift plasmid from F. van Kuppeveld.

Mouse monoclonal antibody anti-CD8a (OKT8) was from the hybridoma culture supernatant. Mouse monoclonal antibodies against GM130 (#610822) and GS15 (#610960) were purchased from BD Bioscience. Rabbit polyclonal antibody against TGN46 was from Abcam (#ab50595). Alexa Fluor 488, 594, and 647-conjugated goat anti-mouse or anti-rabbit secondary antibodies were purchased from Thermo Fisher Scientific.

Small molecules

Nocodazole (#487928; working concentration: 33 μM), BFA (working concentration: 5 μM), and cycloheximide (working concentration: 10 μg/ml) were purchased from Merck, Epicenter Technologies, and Sigma Aldrich, respectively.

Cell culture and transfection

HeLa and 293T cells were maintained in Dulbecco's Modified Eagle's Medium (DMEM) supplemented with 10% fetal bovine serum (FBS) to make it complete DMEM. For cell transfection, Lipofectamine 2000 (Thermal Fisher Scientific) was used per the manufacturer's instructions. For BFA treatment, cells were treated with complete DMEM containing 5 μM BFA for the specified duration. For nocodazole treatment, cells were treated with complete DMEM containing 33 μM nocodazole for 3 h to induce the formation of Golgi ministacks.

Immunofluorescence

Cells for immunofluorescence were grown on No. 1.5 Φ12 mm glass coverslips. They were fixed using 4% paraformaldehyde in phosphate-buffered saline (PBS). Following a PBS wash to remove residual paraformaldehyde, any remaining paraformaldehyde within the cells was neutralized with 100 mM NH_4Cl. The cells were then processed for immunofluorescence labeling by first incubating with mouse or rabbit primary antibodies, followed by Alexa Fluor 488, 594, and/or 647 conjugated goat anti-mouse or anti-rabbit secondary antibodies. Both primary and secondary antibodies were diluted in PBS containing 5% fetal bovine serum, 2% bovine serum albumin, and 0.1% saponin (Sigma-Aldrich). The labeled cells were mounted in the Mowiol mounting medium, composed of 12% Mowiol 4-88 (EMD Millipore), 30% glycerol, and 100 mM Tris pH 8.5. After the mounting medium had dried, the coverslips were sealed with nail polish and stored at - 20°C.

Acquiring *LQ*s

To analyze *LQ*s of intra-Golgi transport RUSH reporters, HeLa cells transiently co-expressing individual GFP-tagged RUSH reporter and GalT-mCherry were cultured in complete DMEM supplemented with16 nM His-tagged streptavidin (in-house purified using Addgene #20860, a gift plasmid from A. Ting)(Howarth et al., 2006). Following a 3 h nocodazole treatment, cells were chased with 50 μM biotin, 10 μg/ml cycloheximide, and 33 μM nocodazole for various durations before fixation.

In another set of experiments to study *LQ*s of Golgi markers under the BFA treatment, nocodazole-treated HeLa cells transiently expressing GalT-mCherry were further incubated with 5 μM BFA and 33 μM nocodazole for various durations before fixation. For these experiments, the Golgi markers were either co-expressed with GalT-mCherry as a GFP-tagged construct or detected as an endogenous protein by immunostaining.

The methodology for acquiring *LQ*s through GLIM has been described in our previous studies(Tie et al., 2017; Tie et al., 2016). Briefly, cells were further immuno-labeled to visualize endogenous GM130. Ministacks exhibiting fluorescence signals of GM130, transfected GalT-mCherry, and the testing protein were imaged using a wide-field microscope. Ministacks were manually selected for analysis, and fluorescence centers for GM130, GalT-mCherry, and the testing protein were acquired using Fiji (https://imagej.net/software/fiji/). After chromatic aberration correction, coordinates of centers were used to calculate *LQ*s, defined as the ratio of axial distances from GM130 to the testing protein and from GM130 to GalT-mCherry. Intra-Golgi transport kinetic *LQ* data were fitted to the first-order exponential function using OriginPro 2020.

In addition to the manual method mentioned above, we employed a newly developed software tool, Auto-GLIM (https://github.com/Chokyotager/AutoGLIM), to automatically analyze our ministack images. To this end, three-color images were acquired as described above. Three z-sections centered around the plane of interest were averaged (average z-projection) for beads and ministacks images. Automated background subtraction was performed using a deep learning segmentation model to first extract the cell contours, followed by a dual

annealing optimization algorithm to perform background subtraction to extract the highest number of valid ROIs according to criteria of GLIM(Tie et al., 2016). Final *LQ*s were further subjected to analysis in OriginPro 2020.

Acquisition of Golgi residence times

The methodology follows protocols previously described(Sun et al., 2021; Sun et al., 2020). Nocodazole was not used in these experiments. Briefly, HeLa cells on a Φ 35mm glass-bottom Petri dish were transiently transfected to co-express a GFP-tagged reporter and GalT-mCherry. For RUSH reporters, cells were treated with 50 μM biotin at 20 °C for 2 h to accumulate the reporter at the Golgi. Live imaging was performed in a CO_2-independent medium (Thermo Fisher Scientific) with 10% FBS, 4 mM glutamine, and 10 μg/ml cycloheximide, using a wide-field microscope until the cellular GFP fluorescence at the Golgi nearly vanished. The resulting time-lapse images were segmented based on GalT-mCherry using Fiji. Total GFP fluorescence within the Golgi was quantified and fitted to the first-order exponential function $y = y0 + A1\exp(-x/t1)$ in OriginPro 2020. Golgi residence time, $t_{1/2}$, was calculated as $0.693*t1$. We only included time-lapse data with adj. $R^2 \geq 0.80$ and acquisition length $\geq 1.33*t_{1/2}$.

VHH-anti-GFP-mCherry internalization assay

6 × His-tagged VHH-anti-GFP-mCherry was purified as previously described(Sun et al., 2021; Sun et al., 2020). In the internalization assay, HeLa cells transiently expressing GFP-tagged reporters were continuously incubated with 5 μg/ml VHH-anti-GFP-mCherry at 37 °C for 8 h. After washing, cells were fixed and imaged.

Microscopy for GLIM and Golgi residence time

Golgi residence times and most *LQ*s were measured using a wide-field microscope based on Olympus IX83. The microscope featured a 100× oil objective lens (NA 1.40), a motorized stage for sample positioning, and automated filter cubes to accommodate different fluorescence

channels. Dichroic mirrors and filters were optimized for GFP/Alexa fluor 488, mCherry/Alexa Fluor 594, and Alexa Fluor 647. Imaging was captured with an sCMOS (scientific complementary metal oxide semiconductor) camera (Neo) by Andor. A 200W metal halide light source (Lumen Pro 200) by Prior Scientific provided illumination. Operational control and data collection were facilitated through Metamorph software by Molecular Devices. The image pixel size is 65 nm. The range of exposure time is 400 – 5000 ms for each channel.

GS15 *LQ*s during the BFA treatment time course were measured using a spinning disk confocal microscope system comprising Olypus IX81 equipped with a 100× oil objective lens (NA 1.45), a piezo z stage, Yokogawa CSU-X1 spinning head, 50 mW solid state lasers (488, 561 and 640 nm)(Sapphire; Coherent Inc., Santa Clara, CA, United States), an electron multiplying charge-coupled device (Evolve; Photometrics, Tucson, AZ, United States), and filters optimized for for GFP/Alexa fluor 488, mCherry/Alexa Fluor 594, and Alexa Fluor 647. The system was controlled by Metamorph software (Molecular Devices). The image pixel size is 89 nm. The range of exposure time is 200 – 500 ms for each channel.

Airyscan microscopy

The Airyscan microscopy was performed using a Zeiss LSM710 confocal microscope, equipped with alpha Plan-Apochromat 100× NA 1.46 objective and the Airyscan module (Carl Zeiss). The system operation was controlled by Zen software (Carl Zeiss). Three lines of laser lights were used, 488, 561, and 640 nm. The emission band was selected to optimize the capture of the emission light while minimizing channel crosstalk. For side averaging, images were acquired under 63× objective (NA 1.40), zoomed in 3.5× to achieve 45 nm pixel size using the SR mode. The pixel dwelling time is 1.16 µs. The raw images were processed by Airyscan Zen software.

Side averaging and en face averaging

En face and side averaging were performed as described previously using Airyscan images(Tie et al., 2018; Tie et al., 2022). Ministacks with en face views were identified by

giantin rings. They were subsequently normalized, expanded, and aligned with the center of the image, followed by averaging using Fiji. The radial mean intensity profile was acquired by Fiji macros (Tie et al., 2018). Ministacks with side views were identified by giantin double puncta and subjected to rotation, expansion, and normalization before averaging in Fiji(Tie et al., 2022). In a side average image, we define the axial position of a Golgi protein *i* as the *y* component of its center of mass coordinate, y_i. In Figure 3E, LQ^{side} of SBP-GFP-collagenX is calculated as below.

$$LQ^{\text{side}} = \frac{y_{\text{SBP-GFP-collagenX}} - y_{\text{GM130}}}{y_{\text{GalT-mCherry}} - y_{\text{GM130}}}$$

$y_{\text{SBP-GFP-collagenX}}$, y_{GM130}, and $y_{\text{GalT-mCherry}}$ are axial positions of SBP-GFP-collagenX, GM130, and GalT-mCherry in their side average images, respectively. y_{GM130}, and $y_{\text{GalT-mCherry}}$ were measured previously(Tie et al., 2022).

In Figure 6G, the distance from GM130 to GalT-mCherry, $d_{(\text{GM130-GalT-mCherry})}$, was measured from individual ministacks with side views. The axial line intensity profile of GM130 or GalT-mCherry was subjected to Gaussian fitting in OriginPro2020 (Analysis>Fitting>Non-Linear Curve Fit). The calculated *Xc* represents the axial position of each protein. $d_{(\text{GM130-GalT-mCherry})}$ of each Golgi ministack is then calculated as

$$d_{GM130-GalT-mCherry} = Xc_{GalT-mCherry} - Xc_{GM130}$$

and subjected to statistical analysis. $d_{(\text{GalT-mCherry-CD8a-furin})}$ in Figure 6H was calculated similarly.

Declaration of interests

The authors declare no competing interests.

Acknowledgment

We want to thank J. Bonifacino (National Institute of Health, USA), F. van Kuppeveld (Utrecht University), M. Lowe (University of Manchester, UK), F. Perez (Institute of Curie, France), and

A. Ting (Stanford University, USA) for sharing DNA plasmids. This project is supported by the Ministry of Education, Singapore, under its Tier 2 MOE-T2EP30221-0001 and Tier 1 RG 25/22.

Table 1

Intra-Golgi transport kinetics of secretory RUSH reporters in Golgi ministacks. See the legend of Figure 2 for details. #1-4 indicate independent replicates. All data were acquired from HeLa cells except for those labeled with "293T", which were acquired using 293T cells. Except for TNFα-SBP-GFP, which uses Ii-streptavidin as the ER hook, all RUSH reporters employ signal sequence fused streptavidin-KDEL as their ER hook. Superscripts 1 and 2 indicate data were re-analyzed from previous publications, (Tie et al., 2016) and (Sun et al., 2020), respectively. WT, wild type. t_{intra} (intra-Golgi transport time), y_0, and adj. R^2 were calculated by fitting measured *LQ* vs. time kinetics data to Equation 1. d*LQ*/d*t* (at *LQ* = 0.40) was calculated by Equation 3, and converted to nm/min by multiplying 274 nm per *LQ* unit. *SD*, standard deviation.

RUSH reporter	t_{intra} (min) Mean ± SD	t_{intra} (min)	y_0	Adj. R^2	d*LQ*/d*t* (at *LQ* = 0.40)	d*LQ*/d*t* (at *LQ* = 0.40) (nm/min)
SBP-GFP-CD59 #1 (293T)	5 ± 4	0.4	0.66	0.94	0.244	66.7
SBP-GFP-CD59 #2 (293T)		7.3	0.63	0.92	0.022	6.0
SBP-GFP-CD59 #3 (293T)		6.8	0.79	0.85	0.040	10.9
TNFα-SBP-GFP[1]	6.4	6.4	1.09	0.94	0.075	20.5
TfR-SBP-GFP	7	7.0	1.16	0.99	0.075	20.6
SBP-GFP-CD8a-furin-Y+AC #1[1]	7 ± 1	4.9	0.83	0.99	0.061	16.7
SBP-GFP-CD8a-furin-Y+AC #2[1]		7.1	1.00	0.99	0.059	16.0
SBP-GFP-CD8a-furin-Y+AC #3[1]		7.7	1.04	0.92	0.058	15.8
SBP-GFP-Tac #1[2]	7 ± 2	6.0	0.86	0.98	0.053	14.6
SBP-GFP-Tac #2		8.2	0.91	0.98	0.043	11.8
SBP-GFP-E-cadherin #1[1]	8 ± 1	7.6	0.98	0.99	0.053	14.5
SBP-GFP-E-cadherin #2[1]		8.7	1.15	0.96	0.060	16.5
SBP-GFP-E-cadherin #3[1]		6.5	1.11	0.98	0.075	20.6
SBP-GFP-collagenX #1	8± 1	9.0	1.00	0.94	0.046	12.7
SBP-GFP-collagenX #2		9.5	0.84	0.97	0.032	8.8
SBP-GFP-collagenX #3		6.9	0.91	0.97	0.051	14.0
SBP-GFP	10.6	10.6	0.74	0.98	0.022	6.1
SBP-GFP-CD8a-furin-YA #1[1]	11 ± 5	5.9	1.49	0.98	0.13	35.0
SBP-GFP-CD8a-furin-YA #2[1]		11.1	1.51	0.93	0.069	19.0
SBP-GFP-CD8a-furin-YA #3[1]		16.3	1.48	0.95	0.046	12.6
SBP-GFP-CD59[1]	13.0	13.0	1.03	0.97	0.034	9.2
SBP-GFP-Tac-TC #1 (293T)	14.2 ± 0.6	14.7	0.95	0.97	0.026	7.1
SBP-GFP-Tac-TC #2 (293T)		14.3	1.00	0.98	0.029	8.0
SBP-GFP-Tac-TC #3 (293T)		13.6	0.98	0.89	0.030	8.1
SBP-GFP-Tac-TC #1[2]	17 ± 3	15.5	1.05	0.97	0.029	8.0
SBP-GFP-Tac-TC #2		19.1	1.16	0.94	0.028	7.6

SBP-GFP-CD8a-furin-WT #1[1]	18 ± 5	23.6	1.63	0.96	0.036	9.9
SBP-GFP-CD8a-furin-WT #2[1]		18.7	1.58	0.97	0.044	12.0
SBP-GFP-CD8a-furin-WT #3[1]		13.1	1.55	0.97	0.061	16.7
SBP-GFP-CD8a-furin-AC #1[1]	21 ± 5	17.9	1.73	0.99	0.052	14.1
SBP-GFP-CD8a-furin-AC #2[1]		26.9	1.50	1.00	0.028	7.8
SBP-GFP-CD8a-furin-AC #3[1]		23.2	1.58	0.96	0.035	9.7
SBP-GFP-CD8a-furin-AC #4[1]		16.8	1.62	0.99	0.050	13.8

Table 2

Golgi residence times of transmembrane secretory cargos and Golgi glycosyltransferases in native Golgi (without nocodazole). Superscripts 1 and 2 indicate data were from previous publications, (Sun et al., 2020) and (Sun et al., 2021), respectively. The RUSH reporter, TNFα-SBP-GFP, employs signal sequence fused streptavidin-KDEL as the ER hook. *n*, the number of quantified cells; SEM, standard error of the mean.

Transmembrane protein	Golgi residence time ($t_{1/2}$)	*n*	SEM
TNFα-SBP-GFP[1]	6.0 min	73	0.4 min
GFP-CD8a[1]	7.8 min	26	0.7 min
TfR-GFP[1]	10 min	12	1 min
GFP-Tac[1]	16 min	45	2 min
SBP-GFP-CD59	16 min	29	2 min
GFP-Tac (5A)[1]	47 min	57	3 min
GFP-CD8a-TC	66 min	19	7 min
GFP-Tac-TC[1]	3.4 h	22	0.3 h
MGAT2-GFP[2]	4.9 h	26	0.5 h
ST6GAL1-GFP[1]	5.3 h	21	0.6 h

References

Ali, M.F., V.B. Chachadi, A. Petrosyan, and P.W. Cheng. 2012. Golgi phosphoprotein 3 determines cell binding properties under dynamic flow by controlling Golgi localization of core 2 N-acetylglucosaminyltransferase 1. *J Biol Chem*. 287:39564-39577.

Bergmann, J.E., and S.J. Singer. 1983. Immunoelectron microscopic studies of the intracellular transport of the membrane glycoprotein (G) of vesicular stomatitis virus in infected Chinese hamster ovary cells. *J Cell Biol*. 97:1777-1787.

Beznoussenko, G.V., S. Parashuraman, R. Rizzo, R. Polishchuk, O. Martella, D. Di Giandomenico, A. Fusella, A. Spaar, M. Sallese, M.G. Capestrano, M. Pavelka, M.R. Vos, Y.G. Rikers, V. Helms, A.A. Mironov, and A. Luini. 2014. Transport of soluble proteins through the Golgi occurs by diffusion via continuities across cisternae. *Elife*. 3.

Boncompain, G., S. Divoux, N. Gareil, H. de Forges, A. Lescure, L. Latreche, V. Mercanti, F. Jollivet, G. Raposo, and F. Perez. 2012. Synchronization of secretory protein traffic in populations of cells. *Nat Methods*. 9:493-498.

Bonfanti, L., A.A. Mironov, Jr., J.A. Martinez-Menarguez, O. Martella, A. Fusella, M. Baldassarre, R. Buccione, H.J. Geuze, A.A. Mironov, and A. Luini. 1998. Procollagen traverses the Golgi stack without leaving the lumen of cisternae: evidence for cisternal maturation. *Cell*. 95:993-1003.

Castle, J.D., J.D. Jamieson, and G.E. Palade. 1972. Radioautographic analysis of the secretory process in the parotid acinar cell of the rabbit. *J Cell Biol*. 53:290-311.

Chen, Y., D.C. Gershlick, S.Y. Park, and J.S. Bonifacino. 2017. Segregation in the Golgi complex precedes export of endolysosomal proteins in distinct transport carriers. *J Cell Biol*. 216:4141-4151.

Cole, N.B., N. Sciaky, A. Marotta, J. Song, and J. Lippincott-Schwartz. 1996. Golgi dispersal during microtubule disruption: regeneration of Golgi stacks at peripheral endoplasmic reticulum exit sites. *Mol Biol Cell*. 7:631-650.

De Matteis, M.A., M. Di Girolamo, A. Colanzi, M. Pallas, G. Di Tullio, L.J. McDonald, J. Moss, G. Santini, S. Bannykh, D. Corda, and et al. 1994. Stimulation of endogenous ADP-ribosylation by brefeldin A. *Proc Natl Acad Sci U S A*. 91:1114-1118.

De Matteis, M.A., and A. Luini. 2008. Exiting the Golgi complex. *Nat Rev Mol Cell Biol*. 9:273-284.

Diao, A., D. Rahman, D.J. Pappin, J. Lucocq, and M. Lowe. 2003. The coiled-coil membrane protein golgin-84 is a novel rab effector required for Golgi ribbon formation. *J Cell Biol*. 160:201-212.

Donaldson, J.G., D. Finazzi, and R.D. Klausner. 1992. Brefeldin A inhibits Golgi membrane-catalysed exchange of guanine nucleotide onto ARF protein. *Nature*. 360:350-352.

Eckert, E.S., I. Reckmann, A. Hellwig, S. Rohling, A. El-Battari, F.T. Wieland, and V. Popoff. 2014. Golgi phosphoprotein 3 triggers signal-mediated incorporation of glycosyltransferases into coatomer-coated (COPI) vesicles. *J Biol Chem*. 289:31319-31329.

Emr, S., B.S. Glick, A.D. Linstedt, J. Lippincott-Schwartz, A. Luini, V. Malhotra, B.J. Marsh, A. Nakano, S.R. Pfeffer, C. Rabouille, J.E. Rothman, G. Warren, and F.T. Wieland. 2009. Journeys through the Golgi--taking stock in a new era. *J Cell Biol*. 187:449-453.

Engel, B.D., M. Schaffer, S. Albert, S. Asano, J.M. Plitzko, and W. Baumeister. 2015. In situ structural analysis of Golgi intracisternal protein arrays. *Proc Natl Acad Sci U S A*. 112:11264-11269.

Ernst, A.M., S.A. Syed, O. Zaki, F. Bottanelli, H. Zheng, M. Hacke, Z. Xi, F. Rivera-Molina, M. Graham, A.A. Rebane, P. Bjorkholm, D. Baddeley, D. Toomre, F. Pincet, and J.E. Rothman. 2018. S-Palmitoylation Sorts Membrane Cargo for Anterograde Transport in the Golgi. *Dev Cell*. 47:479-493 e477.

Fourriere, L., S. Divoux, M. Roceri, F. Perez, and G. Boncompain. 2016. Microtubule-independent secretion requires functional maturation of Golgi elements. *J Cell Sci*. 129:3238-3250.

Glick, B.S., and A. Luini. 2011. Models for Golgi traffic: a critical assessment. *Cold Spring Harb Perspect Biol*. 3:a005215.

670 Gut, A., F. Kappeler, N. Hyka, M.S. Balda, H.P. Hauri, and K. Matter. 1998. Carbohydrate-mediated
671 Golgi to cell surface transport and apical targeting of membrane proteins. *EMBO J*. 17:1919-
672 1929.
673 Helms, J.B., and J.E. Rothman. 1992. Inhibition by brefeldin A of a Golgi membrane enzyme that
674 catalyses exchange of guanine nucleotide bound to ARF. *Nature*. 360:352-354.
675 Hirschberg, K., C.M. Miller, J. Ellenberg, J.F. Presley, E.D. Siggia, R.D. Phair, and J. Lippincott-
676 Schwartz. 1998. Kinetic analysis of secretory protein traffic and characterization of golgi to
677 plasma membrane transport intermediates in living cells. *J Cell Biol*. 143:1485-1503.
678 Howarth, M., D.J. Chinnapen, K. Gerrow, P.C. Dorrestein, M.R. Grandy, N.L. Kelleher, A. El-Husseini,
679 and A.Y. Ting. 2006. A monovalent streptavidin with a single femtomolar biotin binding site.
680 *Nat Methods*. 3:267-273.
681 Klausner, R.D., J.G. Donaldson, and J. Lippincott-Schwartz. 1992. Brefeldin A: insights into the control
682 of membrane traffic and organelle structure. *J Cell Biol*. 116:1071-1080.
683 Klumperman, J. 2011. Architecture of the mammalian Golgi. *Cold Spring Harb Perspect Biol*. 3.
684 Kurokawa, K., H. Osakada, T. Kojidani, M. Waga, Y. Suda, H. Asakawa, T. Haraguchi, and A. Nakano.
685 2019. Visualization of secretory cargo transport within the Golgi apparatus. *J Cell Biol*.
686 218:1602-1618.
687 Kwan, A.P., C.E. Cummings, J.A. Chapman, and M.E. Grant. 1991. Macromolecular organization of
688 chicken type X collagen in vitro. *J Cell Biol*. 114:597-604.
689 Lavieu, G., H. Zheng, and J.E. Rothman. 2013. Stapled Golgi cisternae remain in place as cargo passes
690 through the stack. *Elife*. 2:e00558.
691 Lippincott-Schwartz, J., J.G. Donaldson, A. Schweizer, E.G. Berger, H.P. Hauri, L.C. Yuan, and R.D.
692 Klausner. 1990. Microtubule-dependent retrograde transport of proteins into the ER in the
693 presence of brefeldin A suggests an ER recycling pathway. *Cell*. 60:821-836.
694 Liu, L., B. Doray, and S. Kornfeld. 2018. Recycling of Golgi glycosyltransferases requires direct binding
695 to coatomer. *Proc Natl Acad Sci U S A*. 115:8984-8989.
696 Losev, E., C.A. Reinke, J. Jellen, D.E. Strongin, B.J. Bevis, and B.S. Glick. 2006. Golgi maturation
697 visualized in living yeast. *Nature*. 441:1002-1006.
698 Luini, A. 2011. A brief history of the cisternal progression-maturation model. *Cell Logist*. 1:6-11.
699 Mahajan, D., B.K. Boh, Y. Zhou, L. Chen, T.C. Cornvik, W. Hong, and L. Lu. 2013. Mammalian
700 Mon2/Ysl2 regulates endosome-to-Golgi trafficking but possesses no guanine nucleotide
701 exchange activity toward Arl1 GTPase. *Sci Rep*. 3:3362.
702 Marsh, B.J., N. Volkmann, J.R. McIntosh, and K.E. Howell. 2004. Direct continuities between
703 cisternae at different levels of the Golgi complex in glucose-stimulated mouse islet beta
704 cells. *Proc Natl Acad Sci U S A*. 101:5565-5570.
705 Matsuura-Tokita, K., M. Takeuchi, A. Ichihara, K. Mikuriya, and A. Nakano. 2006. Live imaging of
706 yeast Golgi cisternal maturation. *Nature*. 441:1007-1010.
707 Mironov, A.A., G.V. Beznoussenko, P. Nicoziani, O. Martella, A. Trucco, H.S. Kweon, D. Di
708 Giandomenico, R.S. Polishchuk, A. Fusella, P. Lupetti, E.G. Berger, W.J. Geerts, A.J. Koster,
709 K.N. Burger, and A. Luini. 2001. Small cargo proteins and large aggregates can traverse the
710 Golgi by a common mechanism without leaving the lumen of cisternae. *J Cell Biol*. 155:1225-
711 1238.
712 Monetta, P., I. Slavin, N. Romero, and C. Alvarez. 2007. Rab1b interacts with GBF1 and modulates
713 both ARF1 dynamics and COPI association. *Mol Biol Cell*. 18:2400-2410.
714 Patterson, G.H., K. Hirschberg, R.S. Polishchuk, D. Gerlich, R.D. Phair, and J. Lippincott-Schwartz.
715 2008. Transport through the Golgi apparatus by rapid partitioning within a two-phase
716 membrane system. *Cell*. 133:1055-1067.
717 Pereira, N.A., H.X. Pu, H. Goh, and Z. Song. 2014. Golgi phosphoprotein 3 mediates the Golgi
718 localization and function of protein O-linked mannose beta-1,2-N-
719 acetylglucosaminyltransferase 1. *J Biol Chem*. 289:14762-14770.

720 Pfeffer, S.R. 2010. How the Golgi works: a cisternal progenitor model. *Proc Natl Acad Sci U S A*.
721 107:19614-19618.
722 Popoff, V., F. Adolf, B. Brugger, and F. Wieland. 2011. COPI budding within the Golgi stack. *Cold*
723 *Spring Harb Perspect Biol*. 3:a005231.
724 Rabouille, C., and J. Klumperman. 2005. Opinion: The maturing role of COPI vesicles in intra-Golgi
725 transport. *Nat Rev Mol Cell Biol*. 6:812-817.
726 Rizzo, R., D. Russo, K. Kurokawa, P. Sahu, B. Lombardi, D. Supino, M.A. Zhukovsky, A. Vocat, P.
727 Pothukuchi, V. Kunnathully, L. Capolupo, G. Boncompain, C. Vitagliano, F. Zito Marino, G.
728 Aquino, D. Montariello, P. Henklein, L. Mandrich, G. Botti, H. Clausen, U. Mandel, T. Yamaji,
729 K. Hanada, A. Budillon, F. Perez, S. Parashuraman, Y.A. Hannun, A. Nakano, D. Corda, G.
730 D'Angelo, and A. Luini. 2021. Golgi maturation-dependent glycoenzyme recycling controls
731 glycosphingolipid biosynthesis and cell growth via GOLPH3. *EMBO J*. 40:e107238.
732 Rogalski, A.A., J.E. Bergmann, and S.J. Singer. 1984. Effect of microtubule assembly status on the
733 intracellular processing and surface expression of an integral protein of the plasma
734 membrane. *J Cell Biol*. 99:1101-1109.
735 Schmitz, K.R., J. Liu, S. Li, T.G. Setty, C.S. Wood, C.G. Burd, and K.M. Ferguson. 2008. Golgi
736 localization of glycosyltransferases requires a Vps74p oligomer. *Dev Cell*. 14:523-534.
737 Schueder, F., F. Rivera-Molina, M. Su, Z. Marin, P. Kidd, J.E. Rothman, D. Toomre, and J. Bewersdorf.
738 2024. Unraveling cellular complexity with transient adapters in highly multiplexed super-
739 resolution imaging. *Cell*. 187:1769-1784 e1718.
740 Sun, X., D. Mahajan, B. Chen, Z. Song, and L. Lu. 2021. A quantitative study of the Golgi retention of
741 glycosyltransferases. *J Cell Sci*. 134.
742 Sun, X., H.C. Tie, B. Chen, and L. Lu. 2020. Glycans function as a Golgi export signal to promote the
743 constitutive exocytic trafficking. *J Biol Chem*. 295:14750-14762.
744 Tie, H.C., B. Chen, X. Sun, L. Cheng, and L. Lu. 2017. Quantitative Localization of a Golgi Protein by
745 Imaging Its Center of Fluorescence Mass. *J Vis Exp*.
746 Tie, H.C., A. Ludwig, S. Sandin, and L. Lu. 2018. The spatial separation of processing and transport
747 functions to the interior and periphery of the Golgi stack. *Elife*. 7.
748 Tie, H.C., D. Mahajan, B. Chen, L. Cheng, A.M. VanDongen, and L. Lu. 2016. A novel imaging method
749 for quantitative Golgi localization reveals differential intra-Golgi trafficking of secretory
750 cargoes. *Mol Biol Cell*. 27:848-861.
751 Tie, H.C., D. Mahajan, and L. Lu. 2022. Visualizing intra-Golgi localization and transport by side-
752 averaging Golgi ministacks. *J Cell Biol*. 221.
753 Trucco, A., R.S. Polishchuk, O. Martella, A. Di Pentima, A. Fusella, D. Di Giandomenico, E. San Pietro,
754 G.V. Beznoussenko, E.V. Polishchuk, M. Baldassarre, R. Buccione, W.J. Geerts, A.J. Koster,
755 K.N. Burger, A.A. Mironov, and A. Luini. 2004. Secretory traffic triggers the formation of
756 tubular continuities across Golgi sub-compartments. *Nat Cell Biol*. 6:1071-1081.
757 Tu, L., W.C. Tai, L. Chen, and D.K. Banfield. 2008. Signal-mediated dynamic retention of
758 glycosyltransferases in the Golgi. *Science*. 321:404-407.
759 Van De Moortele, S., R. Picart, A. Tixier-Vidal, and C. Tougard. 1993. Nocodazole and taxol affect
760 subcellular compartments but not secretory activity of GH3B6 prolactin cells. *Eur J Cell Biol*.
761 60:217-227.
762 Volchuk, A., M. Amherdt, M. Ravazzola, B. Brugger, V.M. Rivera, T. Clackson, A. Perrelet, T.H. Sollner,
763 J.E. Rothman, and L. Orci. 2000. Megavesicles implicated in the rapid transport of
764 intracisternal aggregates across the Golgi stack. *Cell*. 102:335-348.
765 Weigel, A.V., C.L. Chang, G. Shtengel, C.S. Xu, D.P. Hoffman, M. Freeman, N. Iyer, J. Aaron, S. Khuon,
766 J. Bogovic, W. Qiu, H.F. Hess, and J. Lippincott-Schwartz. 2021. ER-to-Golgi protein delivery
767 through an interwoven, tubular network extending from ER. *Cell*. 184:2412-2429 e2416.
768 Wessels, E., D. Duijsings, T.K. Niu, S. Neumann, V.M. Oorschot, F. de Lange, K.H. Lanke, J.
769 Klumperman, A. Henke, C.L. Jackson, W.J. Melchers, and F.J. van Kuppeveld. 2006. A viral

770 protein that blocks Arf1-mediated COP-I assembly by inhibiting the guanine nucleotide
771 exchange factor GBF1. *Dev Cell*. 11:191-201.

772

Figure 1

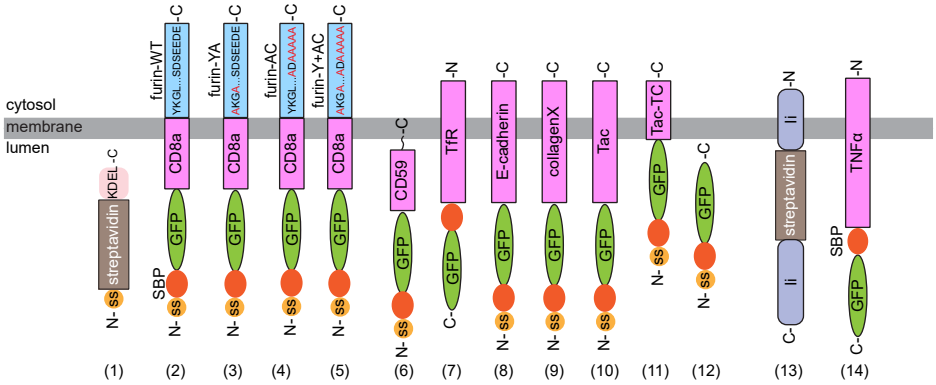
cytosol
membrane
lumen
N- ss
streptavidin
KDEL -C
(1)
furin-WT
YKGL...SDSEEDE
-C
CD8a
GFP
SBP
N- ss
(2)
furin-YA
AKGA...SDSEEDE
-C
CD8a
GFP
N- ss
(3)
furin-AC
YKGL...ADAAAA
-C
CD8a
GFP
N- ss
(4)
furin-Y+AC
AKGA...ADAAAA
-C
CD8a
GFP
N- ss
(5)
CD59
-C
GFP
N- ss
(6)
-N
TfR
GFP
C-
(7)
-C
E-cadherin
GFP
N- ss
(8)
-C
collagenX
GFP
N- ss
(9)
-C
Tac
GFP
N- ss
(10)
Tac-TC
-C
GFP
N- ss
(11)
-C
GFP
N- ss
(12)
-N
Ii
streptavidin
Ii
C-
(13)
-N
TNFα
SBP
GFP
C-
(14)

Figure legends

Figure 1

A schematic diagram showing the domain organizations of ER hooks and RUSH reporters used in this study. (1) streptavidin-KDEL (ER hook), (2) SBP-GFP-CD8a-furin-WT, (3) SBP-GFP-CD8a-furin-YA, (4) SBP-GFP-CD8a-furin-AC, (5) SBP-GFP-CD8a-furin-Y+AC, (6) SBP-GFP-CD59, (7) TfR-SBP-GFP, (8) SBP-GFP-E-cadherin, (9) SBP-GFP-collagenX, (10) SBP-GFP-Tac, (11) SBP-GFP-Tac-TC, (12) SBP-GFP, (13) Ii-streptavidin (ER hook), (14) TNFα-SBP-GFP. ss, signal sequence. SBP, streptavidin binding peptide. (1) is the ER hook for RUSH reporters (2-12), while (13) is the ER Hook for the RUSH reporter (14). Key cytosolic amino acid motifs are indicated for furin cytosolic tail RUSH reporters. YA is YKGL, a tyrosine-based motif, to AKGL mutation, while AC is SDSEEDE, an acidic cluster sequence, to ADAAAAA mutation(Tie et al., 2016). Y + AC indicates mutations in both sites (Tie et al., 2016).

Figure 2

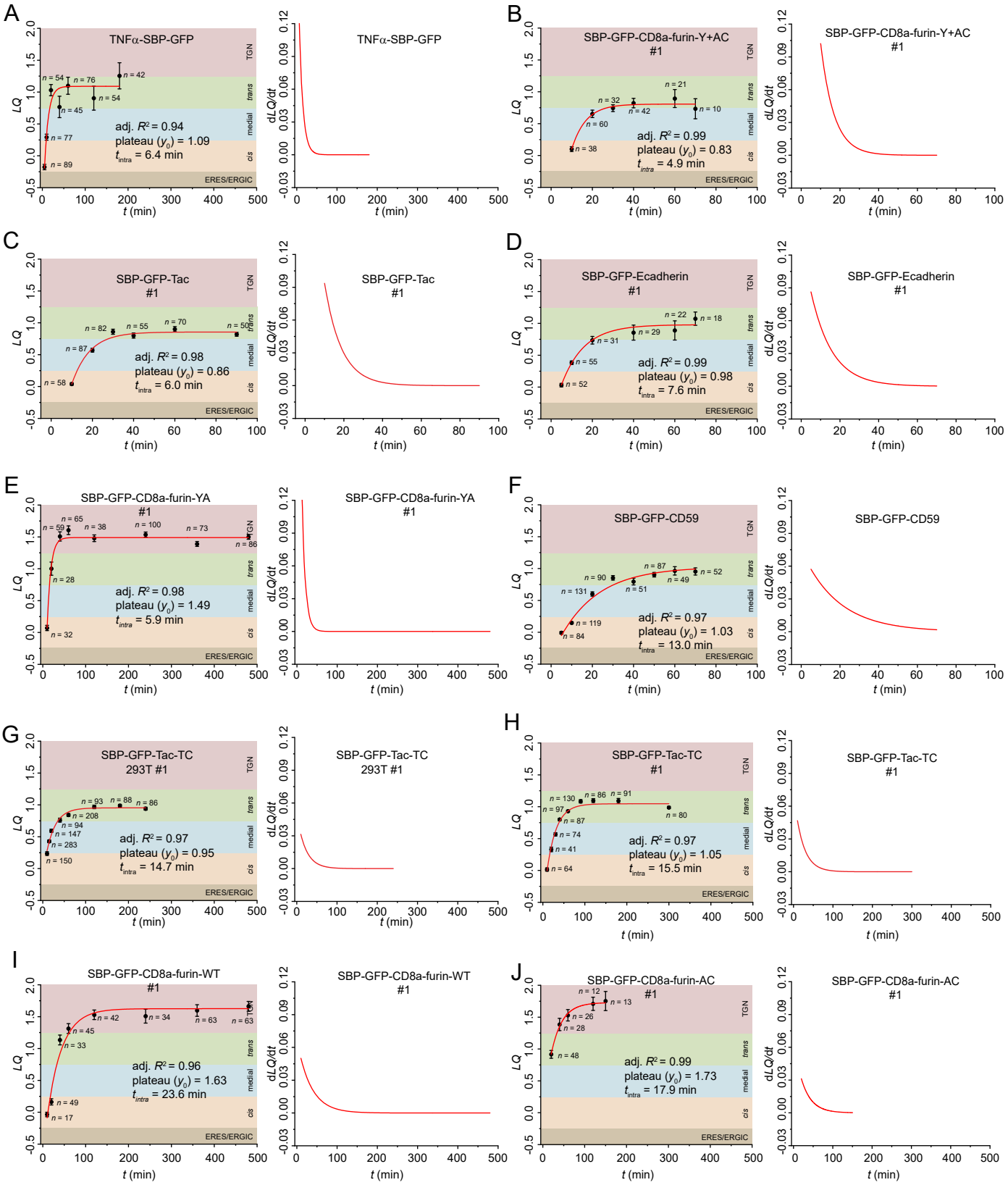
A
TNFα-SBP-GFP
adj. R^2 = 0.94
plateau (y_0) = 1.09
t_{intra} = 6.4 min
B
SBP-GFP-CD8a-furin-Y+AC #1
adj. R^2 = 0.99
plateau (y_0) = 0.83
t_{intra} = 4.9 min
C
SBP-GFP-Tac #1
adj. R^2 = 0.98
plateau (y_0) = 0.86
t_{intra} = 6.0 min
D
SBP-GFP-Ecadherin #1
adj. R^2 = 0.99
plateau (y_0) = 0.98
t_{intra} = 7.6 min
E
SBP-GFP-CD8a-furin-YA #1
adj. R^2 = 0.98
plateau (y_0) = 1.49
t_{intra} = 5.9 min
F
SBP-GFP-CD59
adj. R^2 = 0.97
plateau (y_0) = 1.03
t_{intra} = 13.0 min
G
SBP-GFP-Tac-TC 293T #1
adj. R^2 = 0.97
plateau (y_0) = 0.95
t_{intra} = 14.7 min
H
SBP-GFP-Tac-TC #1
adj. R^2 = 0.97
plateau (y_0) = 1.05
t_{intra} = 15.5 min
I
SBP-GFP-CD8a-furin-WT #1
adj. R^2 = 0.96
plateau (y_0) = 1.63
t_{intra} = 23.6 min
J
SBP-GFP-CD8a-furin-AC #1
adj. R^2 = 0.99
plateau (y_0) = 1.73
t_{intra} = 17.9 min
TGN
trans
medial
cis
ERES/ERGIC
LQ
dLQ/dt
t (min)

Figure 2

The intra-Golgi transport kinetics for RUSH Reporters in Golgi ministacks. HeLa or 293T cells transiently co-expressing individual RUSH reporter and GalT-mCherry were incubated with nocodazole for 3 h. This was followed by a chase with nocodazole, cycloheximide, and biotin for variable time durations (*t*) before fixation and GM130 immunostaining. Except for TNFα-SBP-GFP, which uses Ii-streptavidin as the ER hook, all RUSH reporters employ signal sequence fused streptavidin-KDEL as their ER hook. Using GLIM, *LQ*s for the RUSH reporters were then calculated and plotted. Each panel has an *LQ* vs. *t* plot on the left, with *n* (the number of analyzable Golgi ministacks), adj. R^2, y_0, and t_{intra} indicated. On the right side of each panel, the d*LQ*/d*t* vs. *t* plot represents the first-order derivative of its corresponding *LQ* vs. *t* plot on the left. ERES/ERGIC ($LQ < -0.25$), *cis* ($-0.25 \leq LQ < 0.25$), medial ($0.25 \leq LQ < 0.75$), *trans*-Golgi ($0.75 \leq LQ < 1.25$), and TGN ($1.25 \leq LQ$) zones were color-shaded. The *LQ* vs. *t* plot in panel G was acquired in 293T cells and analyzed by the Auto-GLIM tool, while the rest are from our previous reports (see Table 1). Panels are arranged according to their RUSH reporters' t_{intra} means (see Table 1). See Supplementary File 1 for the raw data.

Figure 3

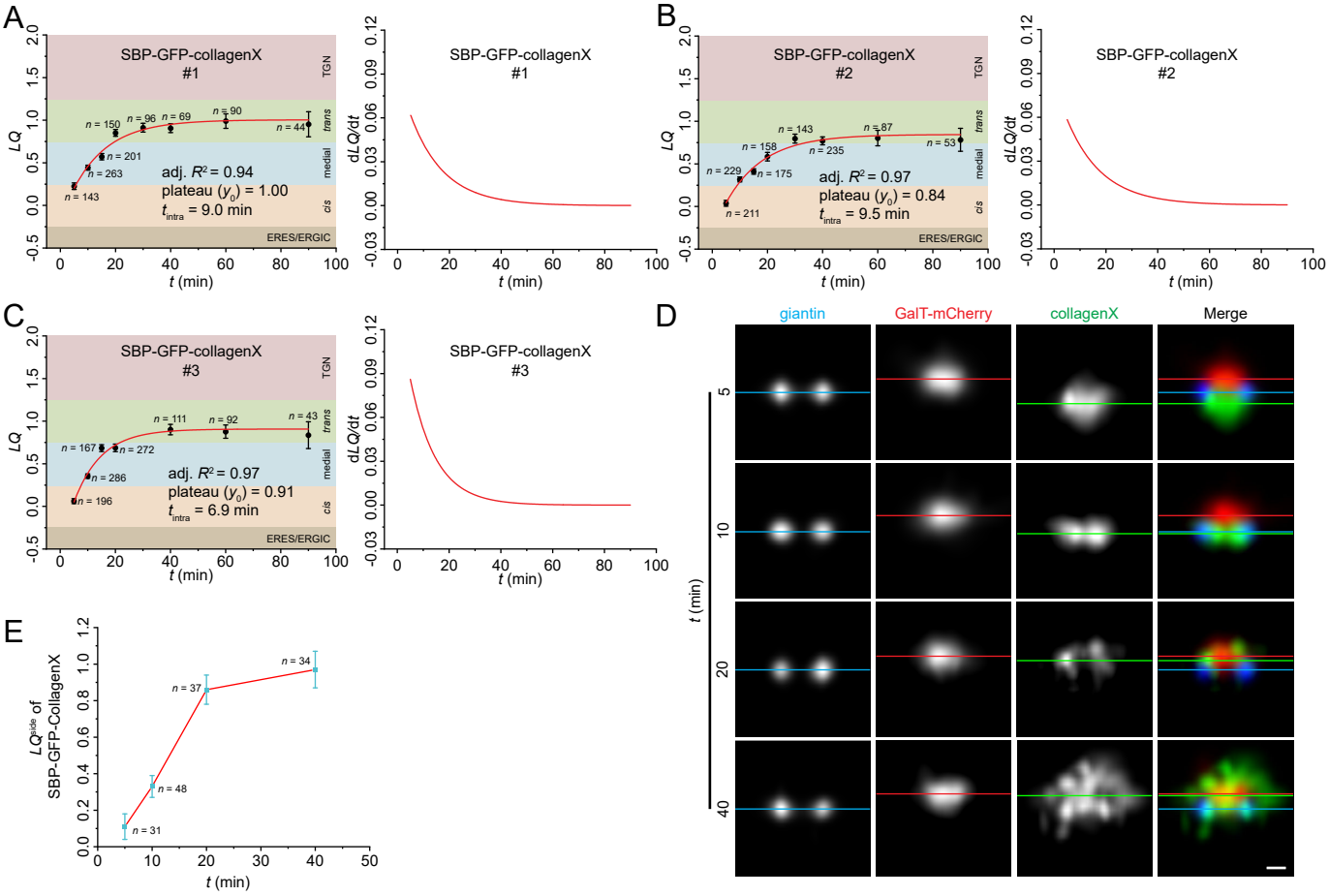
A
SBP-GFP-collagenX
#1
TGN
trans
medial
cis
ERES/ERGIC
n = 143
n = 263
n = 201
n = 150
n = 96
n = 69
n = 90
n = 44
adj. R² = 0.94
plateau (y0) = 1.00
tintra = 9.0 min
LQ
t (min)
dLQ/dt
B
SBP-GFP-collagenX
#2
n = 211
n = 229
n = 175
n = 158
n = 143
n = 235
n = 87
n = 53
adj. R² = 0.97
plateau (y0) = 0.84
tintra = 9.5 min
C
SBP-GFP-collagenX
#3
n = 196
n = 286
n = 167
n = 272
n = 111
n = 92
n = 43
adj. R² = 0.97
plateau (y0) = 0.91
tintra = 6.9 min
D
giantin
GalT-mCherry
collagenX
Merge
t (min)
5
10
20
40
E
LQside of SBP-GFP-CollagenX
n = 31
n = 48
n = 37
n = 34
t (min)

Figure 3

The intra-Golgi transport of SBP-GFP-collagenX quantified by GLIM and visualized by side averaging. (A-C) GLIM. HeLa cells transiently co-expressing the RUSH reporter, SBP-GFP-collagenX, and GalT-mCherry were imaged during biotin chase (*t*) and subjected to GLIM. See Figure 2 legend for details. (D) Side averaging. HeLa cells transiently co-expressing the RUSH reporter, SBP-GFP-collagenX, and GalT-mCherry were incubated with nocodazole for 3 h. This was followed by a chase with nocodazole, cycloheximide, and biotin for variable time durations (*t*) before fixation and giantin immunostaining. Images were acquired using Airyscan microscopy and subjected to side averaging guided by giantin double puncta. Blue, red, and green horizontal lines represent the center of mass positions of giantin, GalT-mCherry, and SBP-GFP-collagenX, respectively. Scale bar, 200 nm. (E) The LQ^{side} vs. biotin chase time (*t*) plot shows the transition of SBP-GFP-collagenX from the *cis* to the *trans*-region of the Golgi ministack. LQ^{side} is an approximate metric corresponding to *LQ* (see Materials and Methods). *n*, the number of ministacks quantified. Error bar, SEM.

Figure 4

A

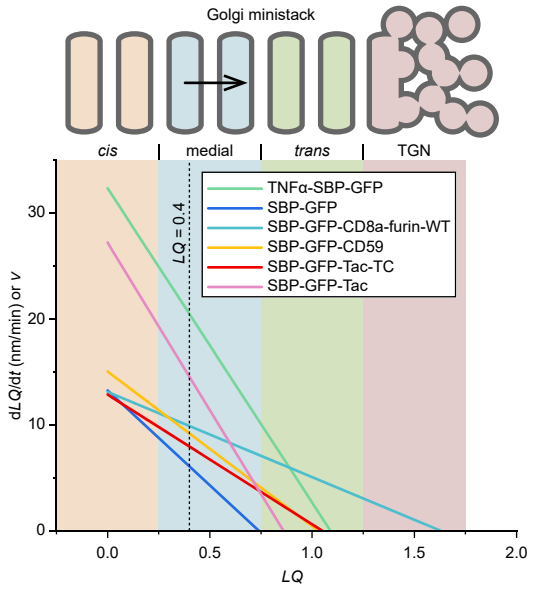
Golgi ministack
cis
medial
trans
TGN
TNFα-SBP-GFP
SBP-GFP
SBP-GFP-CD8a-furin-WT
SBP-GFP-CD59
SBP-GFP-Tac-TC
SBP-GFP-Tac
LQ = 0.4
dLQ/dt (nm/min) or v
LQ
0
10
20
30
0.0
0.5
1.0
1.5
2.0

B

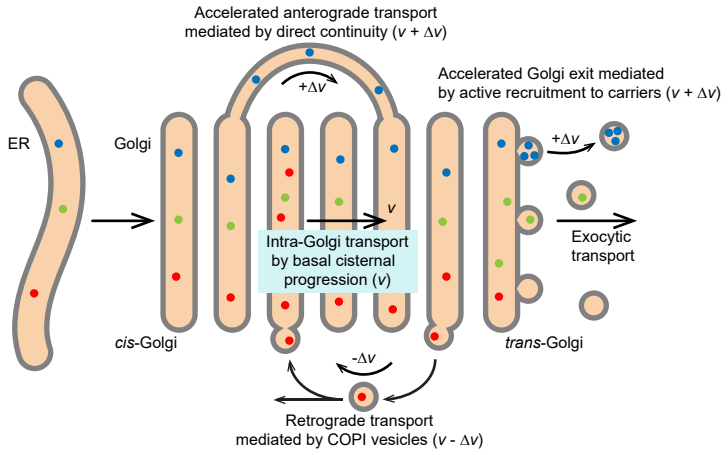
Accelerated anterograde transport
mediated by direct continuity (v + Δv)
+Δv
Accelerated Golgi exit mediated
by active recruitment to carriers (v + Δv)
ER
Golgi
+Δv
v
Intra-Golgi transport
by basal cisternal
progression (v)
Exocytic
transport
cis-Golgi
trans-Golgi
-Δv
Retrograde transport
mediated by COPI vesicles (v - Δv)

Figure 4

Different secretory cargos exhibit distinct intra-Golgi transport velocities within the same cisternae of Golgi ministacks. (A) Plots of d*LQ*/d*t* vs. *LQ* for selected RUSH reporters reveal diverse intra-Golgi transport velocities at the same cisternae. These plots were constructed based on Equation 3, using parameters from Table 1. Different regions within the Golgi — *cis* ($-0.25 \leq LQ < 0.25$), medial ($0.25 \leq LQ < 0.75$), *trans*-Golgi ($0.75 \leq LQ < 1.25$), and TGN ($1.25 \leq LQ$) — are color-shaded for easier identification. To convert d*LQ*/d*t* to nm/min, we multiplied d*LQ*/d*t* by 274 nm per *LQ* unit. A dotted vertical line marks the *LQ* value of 0.40. (B) Modifying the classic cisternal progression model to explain the distinct intra-Golgi transport velocities at the same cisternae. According to this model, Golgi cisternae progress at a constant velocity (v). Direct-continuity-based anterograde transport could accelerate the intra-Golgi transport velocity ($v + \Delta v$), while the COPI-mediated retrograde transport could reduce it ($v - \Delta v$).

Figure 5

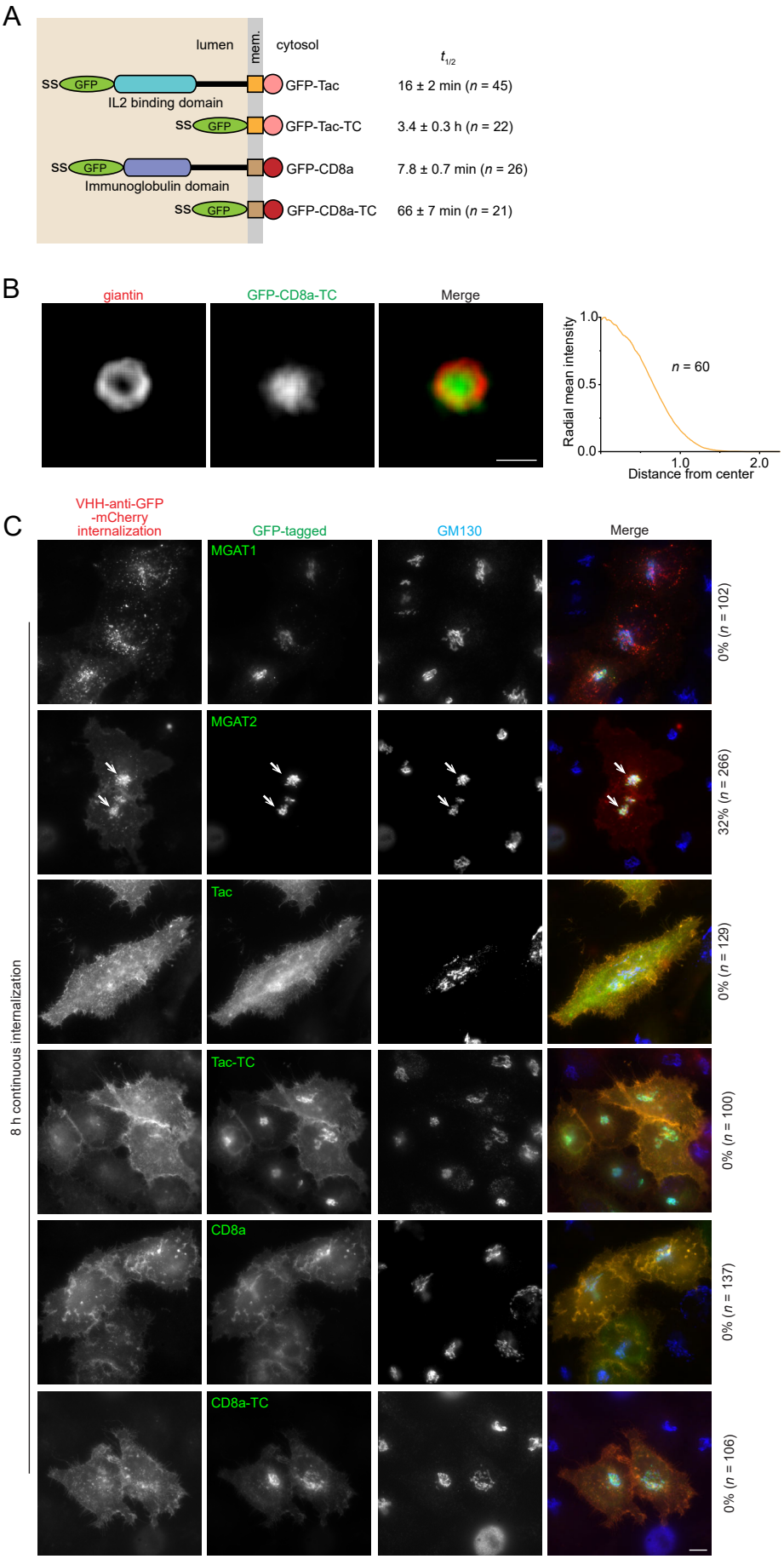
A
lumen
mem.
cytosol
$t_{1/2}$
SS
GFP
IL2 binding domain
GFP-Tac
16 ± 2 min (n = 45)
GFP-Tac-TC
3.4 ± 0.3 h (n = 22)
Immunoglobulin domain
GFP-CD8a
7.8 ± 0.7 min (n = 26)
GFP-CD8a-TC
66 ± 7 min (n = 21)
B
giantin
GFP-CD8a-TC
Merge
Radial mean intensity
1.0
0.5
0.0
n = 60
1.0
2.0
Distance from center
C
VHH-anti-GFP
-mCherry
internalization
GFP-tagged
GM130
Merge
8 h continuous internalization
MGAT1
0% (n = 102)
MGAT2
32% (n = 266)
Tac
0% (n = 129)
Tac-TC
0% (n = 100)
CD8a
0% (n = 137)
CD8a-TC
0% (n = 106)

Figure 5

GFP-Tac-TC and GFP-CD8a-TC might not have a Golgi retrieval mechanism once exiting the Golgi. (A) Domain organization of GFP-tagged Tac, Tac-TC, CD8a, and CD8a-TC. ss, signal sequence. Mem., membrane. $t_{1/2}$ values are from Table 2 and shown as mean ± SEM. *n*, the number of cells analyzed. (B) GFP-CD8a-TC localizes to the Golgi cisternal interior at the steady state. HeLa cells transiently expressing GFP-CD8a-TC were treated with nocodazole to induce the formation of ministacks before fixation and immunostaining for the endogenous giantin. En face averaging images of giantin and GFP-CD8a-TC are shown on the left. Scale bar, 500 nm. The radial mean intensity profile of en face averaged GFP-CD8a-TC is shown on the right. The *x*-axis represents the distance from the center of fluorescence mass (normalized to the giantin radius), and the *y*-axis represents the radial mean intensity (normalized). *n*, the number of averaged ministacks. (C) The plasma membrane-localized GFP-Tac-TC and GFP-CD8a-TC are not retrieved to the Golgi. HeLa cells transiently expressing indicated GFP-tagged protein were incubated continuously with VHH-anti-GFP-mCherry for 8 h before fixation and immunostaining for the endogenous Golgi marker, GM130. Images were acquired under a wide-field microscope. The internalized VHH-anti-GFP-mCherry has negative Golgi localization for all GFP-tagged proteins except for MGAT2 (arrows), a positive control. The percentage of cells showing the Golgi localization of VHH-anti-GFP-mCherry is labeled on the right. *n*, the number of cells analyzed. Scale bar, 10 µm.

Figure 6

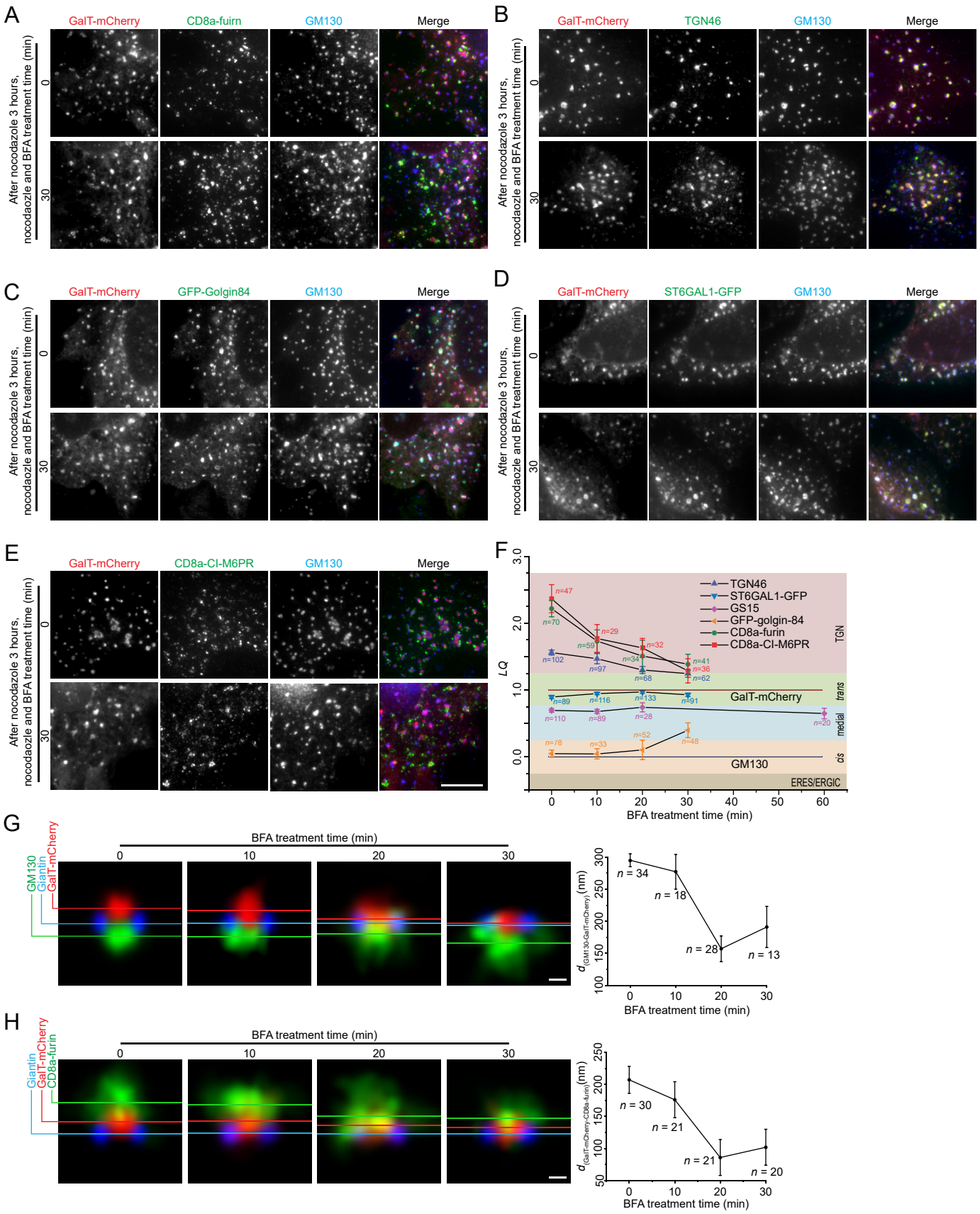
A
GalT-mCherry
CD8a-fuirn
GM130
Merge
After nocodazole 3 hours, nocodaozle and BFA treatment time (min)
0
30
B
GalT-mCherry
TGN46
GM130
Merge
C
GalT-mCherry
GFP-Golgin84
GM130
Merge
D
GalT-mCherry
ST6GAL1-GFP
GM130
Merge
E
GalT-mCherry
CD8a-CI-M6PR
GM130
Merge
F
TGN46
ST6GAL1-GFP
GS15
GFP-golgin-84
CD8a-furin
CD8a-CI-M6PR
GalT-mCherry
GM130
TGN
trans
medial
cis
ERES/ERGIC
LQ
BFA treatment time (min)
G
GM130
Giantin
GalT-mCherry
BFA treatment time (min)
n = 34
n = 18
n = 28
n = 13
BFA treatment time (min)
H
Giantin
GalT-mCherry
CD8a-furin
BFA treatment time (min)
n = 30
n = 21
n = 21
n = 20
BFA treatment time (min)

Figure 6

The organization of Golgi ministacks under the BFA treatment. (A-E) HeLa cells transiently co-expressing GalT-mCherry and indicated GFP or CD8a-tagged Golgi proteins were incubated with nocodazole for 3 h. This was followed by additional treatment with nocodazole and 5 μM BFA for variable durations before fixation. Endogenous TGN46 was immunostained. Images were acquired by wide-field microscopy. Representative images at 0 and 30 min are shown. Scale bar, 10 μm. (F) *LQ*s of different Golgi proteins were determined using GLIM. The dotted lines represent *LQ*s for GM130 (*LQ* = 0.00) and GalT-mCherry (*LQ* = 1.00). *n*, the number of analyzed Golgi ministacks. (G-H) HeLa cells transiently expressing GalT-mCherry alone (G) or together with CD8a-furin (H) were incubated with nocodazole for 3 h. This was followed by additional treatment with nocodazole and 5 μM BFA for variable durations before immunostaining endogenous giantin or GM130. After Airyscan imaging, images were subjected to side averaging. Horizontal color lines indicate centers of mass of corresponding side-averaged Golgi proteins. $d_{(\text{GM130-GalT-mCherry})}$ and $d_{(\text{GalT-mCherry-CD8a-furin})}$ in nm are plotted against the BFA treatment time in the right panels. *n*, the number of ministacks quantified. Error bar, SEM. Scale bar, 200 nm.

Supplementary Figure 1

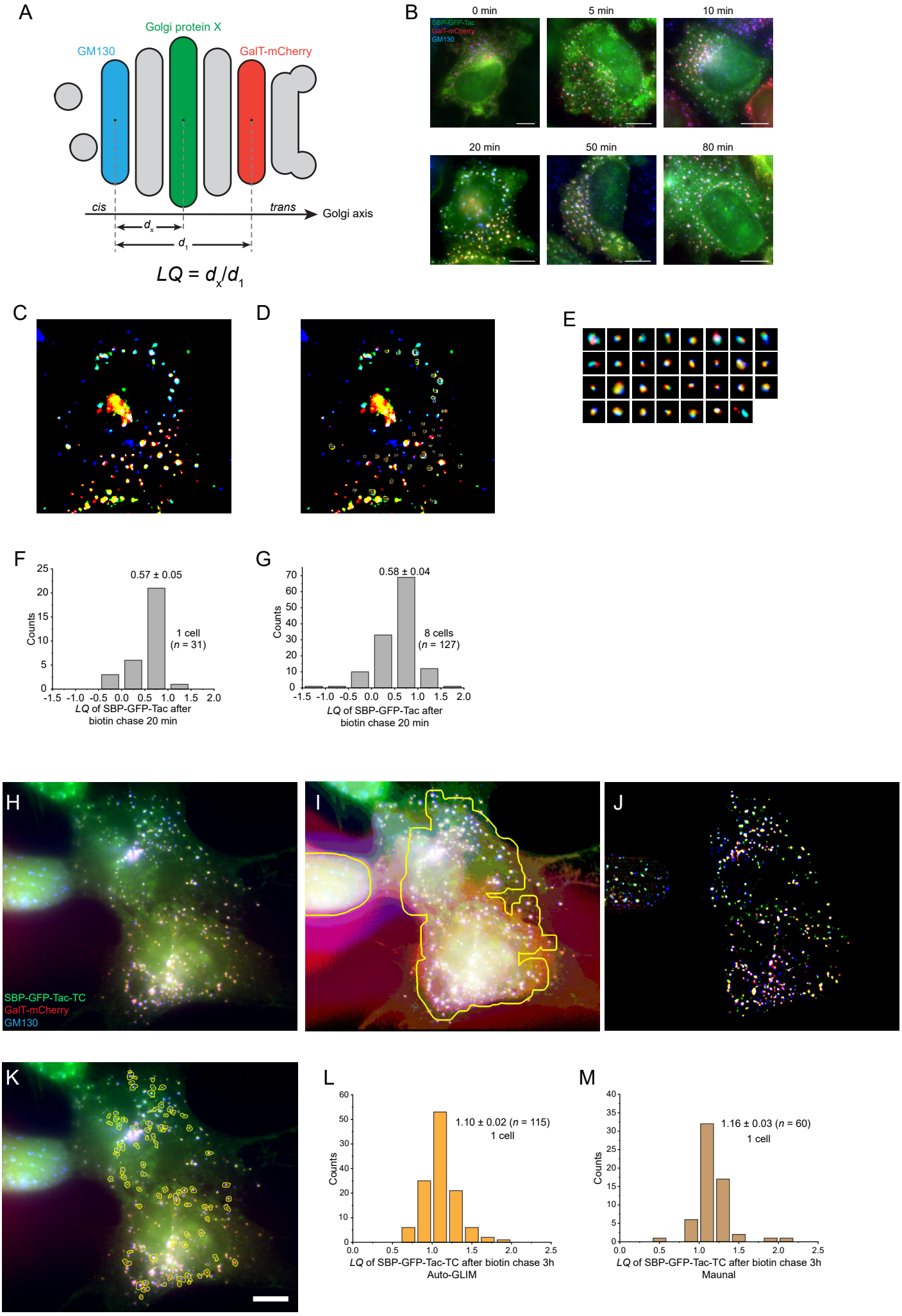

Supplementary information

Supplementary Figure 1

GLIM and the Auto-GLIM tool. (A) A diagram that illustrates the principle behind GLIM. In the Golgi ministack, three proteins, GM130 (endogenous, *cis*-Golgi marker), GalT-mCherry (transfected, *trans*-Golgi marker), and protein X (transfected or endogenous, Golgi protein of interest) are fluorescently labeled. The centers of fluorescence mass (centers) of the three proteins can be calculated. The Golgi axis is defined as the vector from the center of GM130 to that of GalT-mCherry. The distance from the center of GM130 to that of GalT-mCherry is denoted as $d1$, while the distance from the center of GM130 to that of protein X is dx. The LQ is then calculated as d_x/d_1. (B-E) An example that illustrates the study of intra-Golgi transport kinetics using the RUSH reporter (SBP-GFP-Tac) and GLIM. HeLa cells co-expressing SBP-GFP-Tac and GalT-mCherry were treated with nocodazole for 3 h, followed by a biotin chase for various durations. Cells were then immunostained for endogenous GM130 and imaged using wide-field microscopy (B). Scale bar, 10 µm. The image acquired after 20 min biotin chase was selected to demonstrate the image processing for GLIM. The background-subtracted image is displayed in binary intensity to enhance the visualization of ministacks with varying intensities (C). Analyzable ministacks (outlined by yellow contours) were manually selected after intensity thresholding (D). A gallery of 31 analyzable ministacks from (D) and the corresponding LQ histogram (n = 1 cell) are shown in (E) and (F), respectively. The LQ histogram of n = 8 cells is shown in (G). (H-M) Assessing the Auto-GLIM tool. HeLa cells co-expressing GalT-mCherry and SBP-GFP-Tac-TC were treated with nocodzole for 3 h, fixed, and immunostained for endogenous GM130. The image in (H) was acquired by wide-field microscopy. It is subjected to the Auto-GLIM tool with a frame of 72 × 72 pixels to detect the cell contour (marked by the yellow line) (I), conduct background-subtraction (J), and select analyzable Golgi ministacks (marked by yellow lines) (K). Scale bar, 10 µm. The resulting histogram of LQs is shown in (L). We also acquired LQs using the conventional manual method (M), demonstrating strong agreement between the two approaches.

Supplementary Figure 2

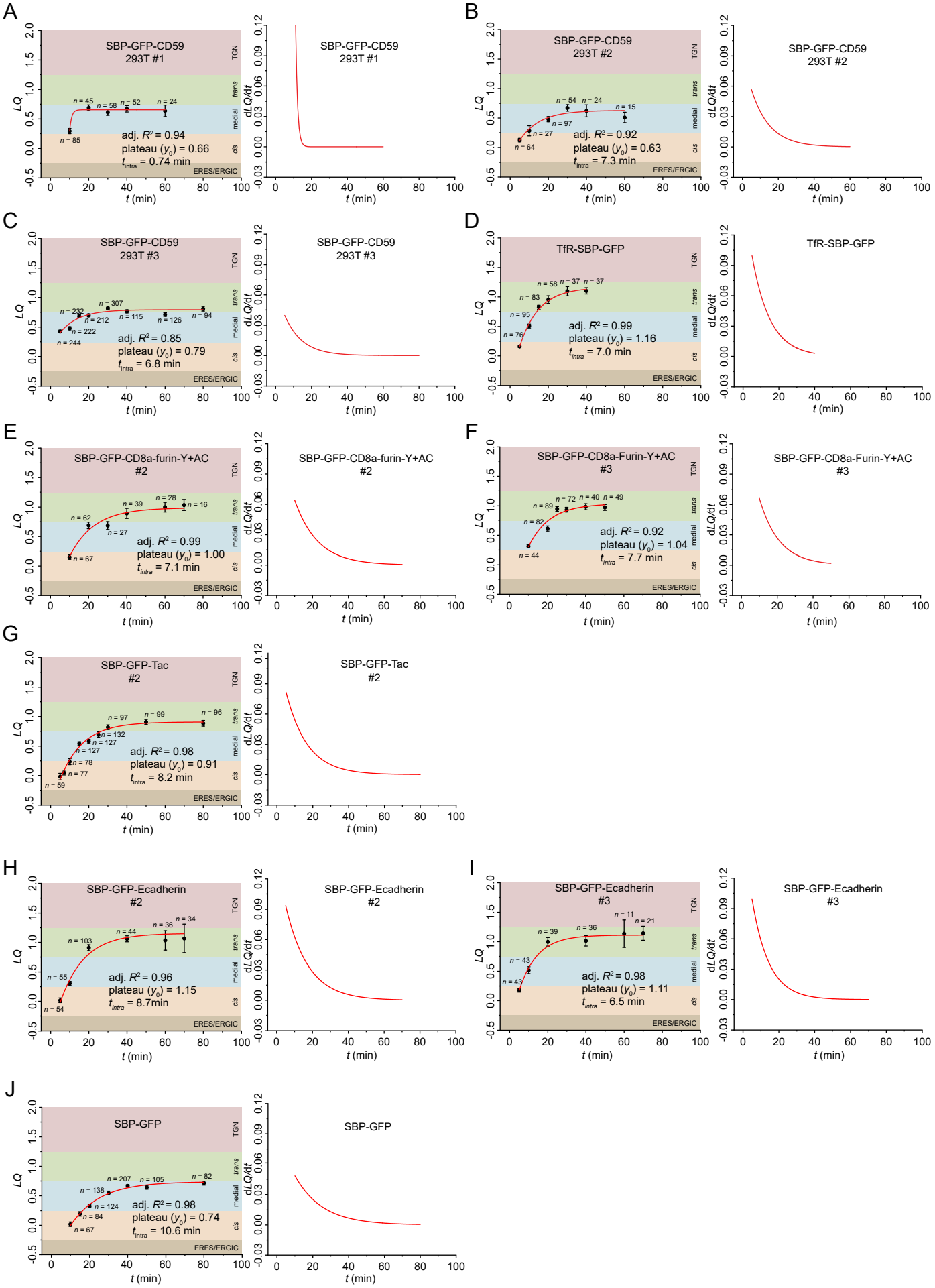

Supplementary Figure 2

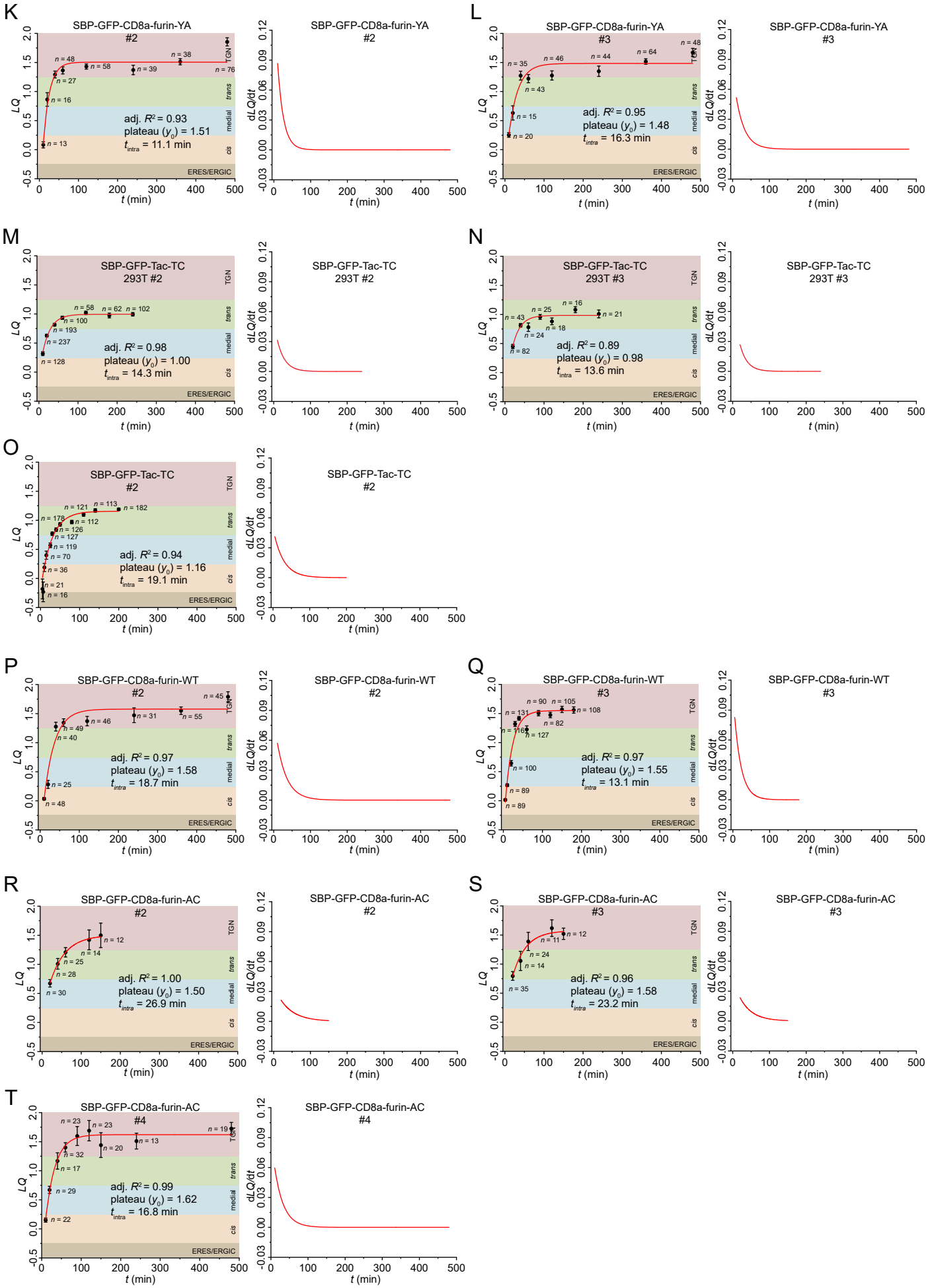

Supplementary Figure 2

Additional intra-Golgi transport kinetics of RUSH reporters. *LQ* vs. *t* plots in (A-D, G, J, and M-O) are generated in this study while the rest are from our previous reports (see Table 1). See the legend of Figure 2 for details.

Supplementary Figure 3

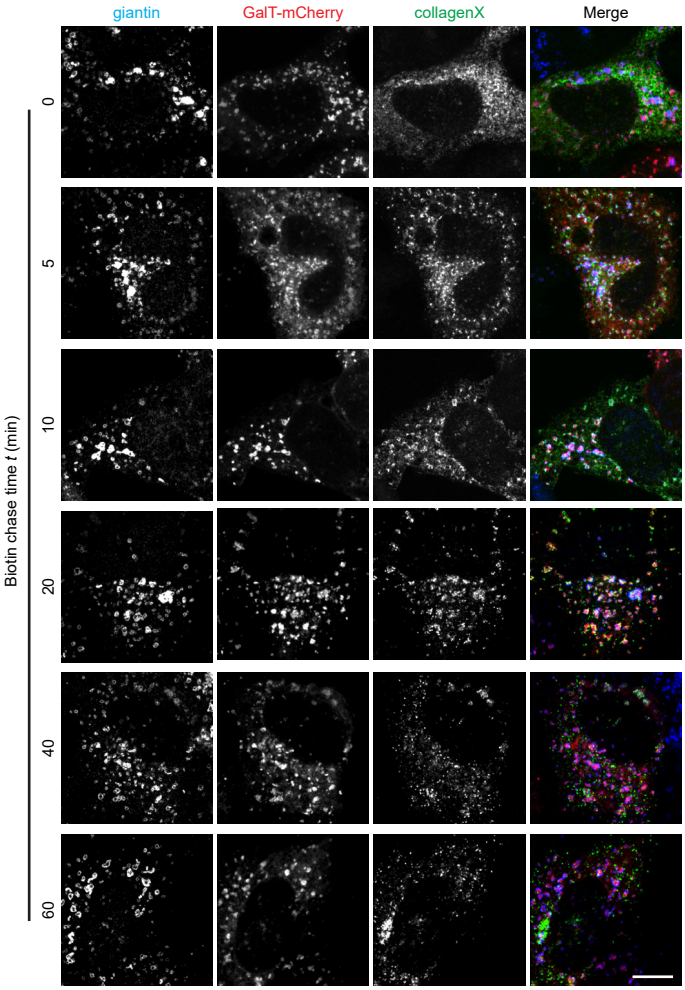

Supplementary Figure 3

Example images used for side averaging in Figure 3D. See the legend of Figure 3D for details. Scale bar, 10 µm.

Supplementary Figure 4

A

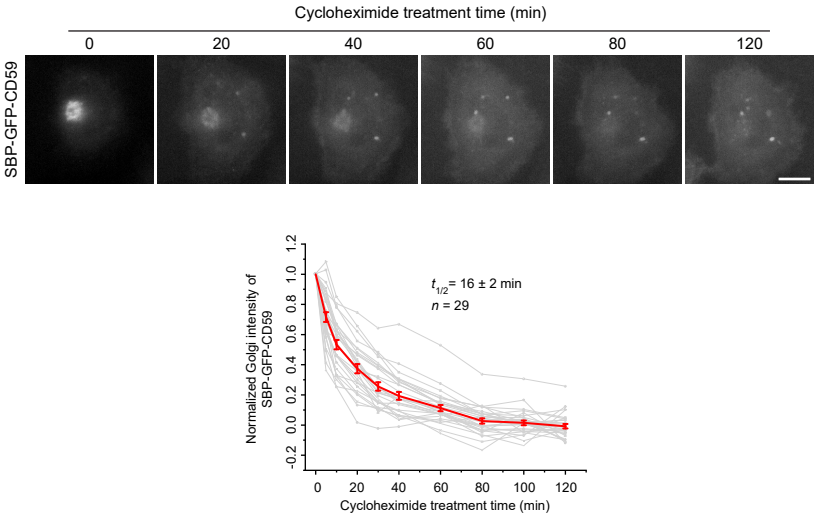

B

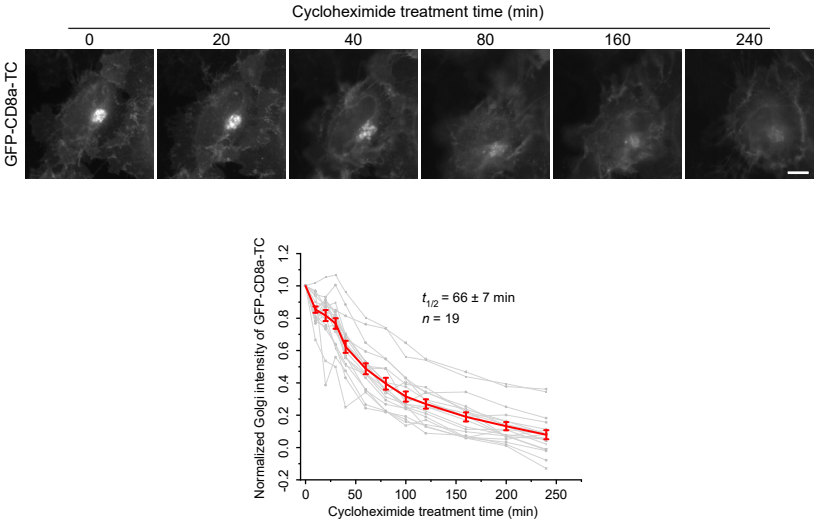

Supplementary Figure 4

Acquiring Golgi residence times of SBP-GFP-CD59 and GFP-CD8a-TC. (A) HeLa cells were transiently transfected to co-express RUSH reporter, SBP-GFP-CD59, and GalT-mCherry. Cells were incubated with biotin and cycloheximide at 20 °C to accumulate the RUSH reporter in the Golgi before live-cell imaging under a wide-field microscope at 37 °C. Only SBP-GFP-CD59 images are shown. (B) HeLa cells transiently co-expressing GFP-CD8a-TC and GalT-mCherry were treated with cycloheximide and imaged live under a wide-field microscope. Only GFP-CD8a-TC images are shown. In both (A) and (B), the total fluorescence intensity within the Golgi was quantified, normalized, and plotted against the time. Each intensity series was fitted to the first-order exponential function to calculate $t_{1/2}$. Grey and red indicate individual and averaged time series, respectively. $t_{1/2}$ is expressed as mean ± SEM. *n*, the number of quantified cells. Scale bar, 10 μm.

Supplementary Figure 5

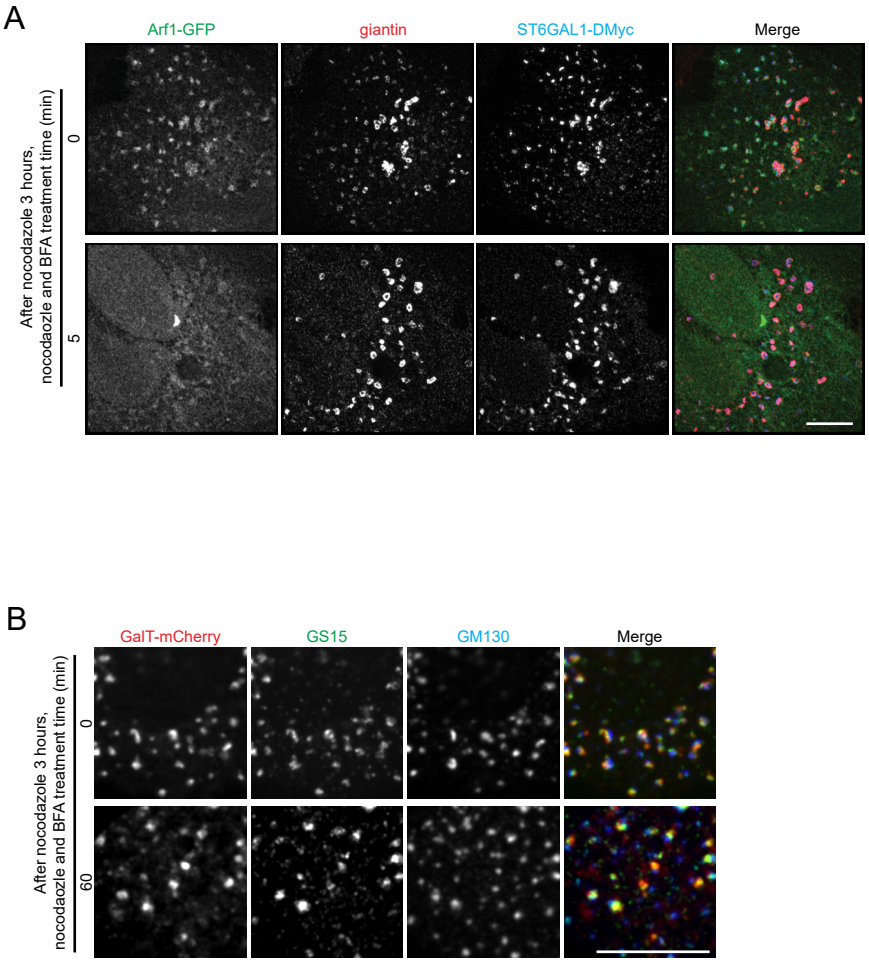

Supplementary Figure 5

The effect of BFA treatment on Golgi markers. (A) Arf1 quickly dissociates from the Golgi under the treatment of nocodazole and BFA. HeLa cells transiently expressing Arf1-GFP and ST6GAL1-DMyc were treated with nocodazole for 3 h. This was followed by additional treatment with nocodazole and 5 µM BFA for 5 min before fixation and immunostaining of Myc-tag and endogenous giantin. Images were acquired by Airyscan microscopy. (B) HeLa cells transiently expressing GalT-mCherry were treated with nocodazole for 3 h. This was followed by additional treatment with nocodazole and 5 µM BFA for variable durations before fixation and immunostaining endogenous GS15 and GM130. Images were acquired by spinning disk confocal microscopy. Representative images at 0 and 60 min are shown. Scale bar, 10 µm.

Supplementary File 1

LQ data employed in plots presented in Figure 2, Figure 6, and Supplementary Figure 2. *n*, the number of quantified cells. SEM, standard error of the mean.

Supplementary File 1

Fig. 2

	Chase time (min)	*n*	*LQ*	SEM	Cell number
A. SBP-TNFa-GFP	5	89	-0.18	0.04	12
	10	77	0.29	0.05	15
	20	54	1.03	0.09	15
	40	45	0.77	0.17	30
	60	76	1.10	0.13	38
	120	54	0.90	0.19	29
	180	42	1.25	0.21	27
B. SBP-GFP-CD8a-furin-Y+AC #1	10	38	0.10	0.04	9
	20	60	0.65	0.06	9
	30	32	0.74	0.05	7
	40	42	0.82	0.07	14
	60	21	0.89	0.14	8
	70	10	0.73	0.16	9
C. SBP-GFP-Tac	10	58	0.04	0.02	4
	20	87	0.57	0.03	3
	30	82	0.86	0.04	6
	40	55	0.80	0.04	2
	60	70	0.90	0.04	3
	90	50	0.82	0.03	2
D. SBP-GFP-Ecadherin #1	5	52	0.03087	0.02753	11
	10	55	0.38	0.03	15
	20	31	0.74	0.06	14
	40	29	0.85	0.12	11
	60	22	0.89	0.15	11
	70	18	1.07	0.10	11
E. SBP-GFP-CD8a-furin-YA #2	10	13	0.08	0.05	11
	20	16	0.86	0.12	10
	40	27	1.29	0.06	16
	60	48	1.36	0.06	11
	120	58	1.43	0.04	6
	240	39	1.37	0.08	11
	360	38	1.51	0.05	10
	480	76	1.85	0.07	5
F. SBP-GFP-CD59	5	84	-0.01	0.02	12
	10	119	0.15	0.02	19
	20	131	0.60	0.03	16
	30	90	0.85	0.04	18
	40	51	0.80	0.05	10
	50	87	0.90	0.04	15
	60	49	0.96	0.07	15
	70	52	0.95	0.06	12
	10	150	0.24	0.03	14
	15	283	0.43	0.02	14

G. SBP-GFP-Tac-TC 293T	20	147	0.59	0.03	11
	40	94	0.76	0.03	8
	60	208	0.84	0.02	13
	120	93	0.97	0.03	10
	180	88	0.99	0.02	9
	240	86	0.94	0.02	10
H. SBP-GFP-Tac-TC	10	64	0.02	0.03	2
	20	41	0.33	0.04	5
	30	74	0.57	0.03	3
	40	87	0.80	0.02	5
	60	97	0.93	0.02	6
	90	130	1.08	0.03	5
	120	86	1.10	0.03	2
	180	91	1.09	0.04	4
	300	80	0.99	0.02	2
I. SBP-GFP-CD8a-furin-WT #1	10	17	-0.03	0.04	14
	20	49	0.16	0.05	16
	40	33	1.13	0.08	14
	60	45	1.31	0.08	10
	120	42	1.53	0.07	10
	240	34	1.51	0.11	17
	360	63	1.60	0.09	18
	480	63	1.66	0.08	16
J. SBP-GFP-CD8a-furin-AC #1	20	48	0.92	0.06	11
	40	28	1.38	0.10	23
	60	26	1.53	0.09	21
	120	12	1.71	0.10	21
	150	13	1.75	0.15	11

Fig. 3

A. SBP-GFP-Collagen X #1

Chase time (min)	*n*	*LQ*	SEM	Cell number
5	143	0.23	0.04	11
10	263	0.44	0.03	17
15	201	0.57	0.04	11
20	150	0.85	0.04	12
30	96	0.91	0.05	9
40	69	0.91	0.05	10
60	90	0.99	0.08	13
90	44	0.95	0.15	11

B. SBP-GFP-Collagen X #2

5	211	0.04	0.03	11
10	229	0.32	0.03	11
15	175	0.41	0.03	8
20	158	0.59	0.05	9
30	143	0.80	0.05	15
40	235	0.77	0.05	15
60	87	0.80	0.09	16
90	53	0.78	0.13	12

C. SBP-GFP-Collagen X #3

5	196	0.06	0.03	8
10	286	0.36	0.03	15
15	167	0.68	0.04	9
20	272	0.69	0.04	14
40	111	0.90	0.06	13
60	92	0.88	0.08	13
90	43	0.84	0.16	13

E. SBP-GFP-Collagen X side-averaging

Chase time (min)	*n*	LQ^{side}	SEM	Cell number
5	31	0.11	0.07	10
10	48	0.33	0.06	10
20	37	0.86	0.08	8
40	34	0.97	0.10	8

Fig. 6

	BFA treatment time(min)	*n*	*LQ*	SEM	Cell number
TGN46	0	102	1.56	0.04	5
	10	97	1.47	0.08	18
	20	68	1.30	0.05	13
	30	62	1.25	0.05	19
ST6GAL1-moxGFP	0	89	0.90	0.03	8
	10	116	0.95	0.02	7
	20	133	0.97	0.02	17
	30	91	0.93	0.03	12
GS15	0	110	0.70	0.03	9
	10	89	0.68	0.03	10
	20	28	0.74	0.07	11
	60	20	0.65	0.08	12
GFP-Golgin-84	0	78	0.05	0.05	8
	10	33	0.04	0.08	15
	20	52	0.10	0.15	14
	30	48	0.40	0.11	13
CD8a-furin	0	70	2.22	0.12	9
	10	59	1.73	0.17	18
	20	34	1.51	0.24	16
	30	41	1.39	0.15	19
CD8a-CI-M6PR	0	47	2.37	0.21	15
	10	29	1.77	0.21	19
	20	32	1.63	0.14	12
	30	36	1.29	0.18	19

	BFA treatment time(min)	*n*	*d*	SEM	Cell number
$d_{(\text{GM130-GalTmCherry})}$ side-averaging	0	34	300	10	9
	10	18	280	27	11
	20	28	160	20	15
	30	13	190	32	7

	BFA treatment time(min)	*n*	*d*	SEM	Cell number
$d_{(\text{GalTmCherry-CD8afurin})}$ side-averaging	0	30	210	21	7
	10	21	180	28	10
	20	21	90	28	9
	30	20	100	28	10

Fig. S2

	Chase time (min)	*n*	*LQ*	SEM	Cell number
A. SBP-GFP-CD59 293T#1	10	85	0.29	0.04	10
	20	45	0.69	0.05	7
	30	58	0.61	0.05	5
	40	52	0.67	0.05	7
	60	24	0.64	0.10	5
B. SBP-GFP-CD59 293T#2	5	64	0.12	0.03	15
	10	27	0.28	0.09	8
	20	97	0.48	0.04	16
	30	54	0.67	0.06	10
	40	24	0.62	0.10	11
	60	15	0.51	0.09	12
C. SBP-GFP-CD59 293T#3	5	244	0.43	0.02	13
	10	222	0.48	0.03	12
	15	232	0.68	0.02	14
	20	212	0.70	0.03	15
	30	307	0.82	0.02	16
	40	115	0.76	0.03	8
	60	126	0.71	0.03	16
	80	94	0.81	0.04	9
D.TfR-SBP-GFP	5	76	0.16	0.02	10
	10	95	0.51	0.03	8
	15	83	0.82	0.03	11
	20	58	0.95	0.06	10
	30	37	1.10	0.08	10
	40	37	1.10	0.05	13
E. SBP-GFP-CD8a-furin-Y+AC #2	10	67	0.15	0.04	13
	20	62	0.69	0.06	11
	30	27	0.68	0.07	13
	40	39	0.89	0.09	14
	60	28	1.00	0.08	15
	70	16	1.04	0.09	13
F. SBP-GFP-CD8a-furin-Y+AC #3	10	44	0.31	0.03	9
	20	82	0.62	0.04	12
	25	89	0.95	0.04	11
	30	72	0.94	0.04	15
	40	40	0.99	0.05	14
	50	49	0.97	0.05	14
G. SBP-GFP-Tac #2	5	59	-0.02	0.06	12
	7	77	0.05	0.04	12
	10	78	0.23	0.05	13
	15	127	0.54	0.03	15
	20	127	0.58	0.04	13
	25	132	0.70	0.04	14

	30	97	0.82	0.04	10
	50	99	0.91	0.04	13
	80	96	0.89	0.05	12
H. SBP-GFP-Ecadherin #2	5	54	0.02	0.04	12
	10	55	0.31	0.04	16
	20	103	0.91	0.05	15
	40	44	1.06	0.05	13
	60	36	1.03	0.17	13
	70	34	1.07	0.24	13
I. SBP-GFP-Ecadherin #3	5	43	0.18	0.03	10
	10	43	0.52	0.06	12
	20	39	1.00	0.07	8
	40	36	1.01	0.09	16
	60	11	1.14	0.23	9
	70	21	1.14	0.12	13
J. SBP-GFP	10	67	0.02	0.04	6
	15	84	0.19	0.04	9
	20	124	0.33	0.02	6
	30	138	0.55	0.03	10
	40	207	0.67	0.02	10
	50	105	0.64	0.03	8
	80	82	0.71	0.03	9
K. SBP-GFP-CD8a-furin-YA #2	10	32	0.07	0.04	5
	20	28	1.00	0.10	6
	40	59	1.51	0.07	12
	60	65	1.61	0.07	11
	120	38	1.48	0.05	6
	240	100	1.54	0.04	11
	360	73	1.39	0.04	11
	480	86	1.50	0.04	5
L. SBP-GFP-CD8a-furin-YA #3	10	20	0.25	0.04	15
	20	15	0.63	0.12	14
	40	35	1.27	0.08	13
	60	43	1.22	0.07	10
	120	46	1.28	0.08	6
	240	44	1.35	0.09	16
	360	64	1.52	0.05	8
	480	48	1.67	0.07	6
M. SBP-GFP-Tac-TC 293T#2	10	128	0.32	0.03	15
	20	237	0.63	0.02	13
	40	193	0.82	0.02	13
	60	100	0.94	0.03	7
	120	58	1.02	0.03	10
	180	62	0.97	0.04	15
	240	102	0.99	0.03	13

N. SBP-GFP-Tac-TC 293T#3	20	83	0.45	0.04	24
	40	43	0.81	0.03	15
	60	24	0.78	0.07	8
	90	25	0.96	0.04	7
	120	18	0.88	0.06	8
	180	16	1.08	0.05	4
	240	21	1.01	0.07	11
O. SBP-GFP-Tac-TC #2	5	21	-0.18	0.17	11
	7	16	-0.23	0.17	9
	10	36	0.19	0.07	12
	15	70	0.40	0.07	9
	25	119	0.69	0.09	11
	30	127	0.77	0.03	10
	40	126	0.84	0.03	10
	50	178	0.93	0.03	11
	80	112	0.99	0.02	9
	110	121	1.11	0.03	9
	140	113	1.18	0.03	12
	200	182	1.19	0.02	11
P. SBP-GFP-CD8a-furin-WT #2	10	48	0.04	0.02	8
	20	25	0.28	0.07	9
	40	40	1.28	0.08	10
	60	49	1.34	0.07	15
	120	46	1.37	0.08	13
	240	31	1.47	0.13	11
	360	55	1.55	0.06	14
	480	45	1.79	0.09	10
Q. SBP-GFP-CD8a-furin-WT #3	5	89	0.02	0.02	9
	10	89	0.27	0.02	10
	20	100	0.64	0.05	8
	30	116	1.32	0.04	18
	40	131	1.42	0.03	9
	60	127	1.23	0.06	17
	90	90	1.51	0.05	9
	120	82	1.47	0.05	17
	150	105	1.57	0.05	13
	180	108	1.56	0.05	13
R. SBP-GFP-CD8a-furin-AC #2	20	30	0.67	0.06	9
	40	28	1.01	0.09	8
	60	25	1.21	0.08	7
	120	14	1.42	0.17	9
	150	12	1.50	0.21	7
S. SBP-GFP-CD8a-furin-AC #3	20	35	0.80	0.07	10
	40	14	1.06	0.17	10
	60	24	1.39	0.16	15
	120	11	1.62	0.14	8
	150	12	1.52	0.10	11

	10	22	0.15	0.04	12
	20	29	0.67	0.06	15
	40	17	1.17	0.14	18
	60	32	1.40	0.08	19
T. SBP-GFP-CD8a-furin-AC #4	90	23	1.60	0.16	17
	120	23	1.69	0.18	17
	150	20	1.44	0.21	11
	240	13	1.51	0.14	10
	480	19	1.73	0.11	8